Angewandte Chemie
Eine Zeitschrift der Gesellschaft Deutscher Chemiker

Supporting Information

Localized and Collective Motions in HET-s(218-289) Fibrils from Combined NMR Relaxation and MD Simulation

Albert A. Smith, Matthias Ernst, Sereina Riniker,* and Beat H. Meier**

anie_201901929_sm_miscellaneous_information.pdf

Table of Contents

1. Methods

1.1. Detector analysis of HET-s(218-289) data

Detector analysis is performed by fitting experimental data to a set of detection vectors,[1] using the DIFRATE software.[2] Detection vectors ($\vec{r}_n$) were optimized to yield the sensitivities shown in Figs. 1A and 4A (main text). We solve the following equation for:

$$\begin{pmatrix} R_{1\rho,10}/\sigma_{R1\rho,10} \\ R_{1\rho,16}/\sigma_{R1\rho,16} \\ R_{1\rho,25}/\sigma_{R1\rho,25} \\ R_{1\rho,38}/\sigma_{R1\rho,38} \\ R_{1\rho,51}/\sigma_{R1\rho,51} \\ R_{1,400}/\sigma_{R1,400} \\ R_{1,500}/\sigma_{R1,500} \\ R_{1,850}/\sigma_{R1,850} \\ 1-S^2/\sigma_{S^2} \end{pmatrix} = \begin{pmatrix} [\vec{r}_0]_{R1\rho,10}/\sigma_{R1\rho,10} & [\vec{r}_1]_{R1\rho,10}/\sigma_{R1\rho,10} & \cdots & [\vec{r}_5]_{R1\rho,10}/\sigma_{R1\rho,10} \\ [\vec{r}_0]_{R1\rho,16}/\sigma_{R1\rho,16} & [\vec{r}_1]_{R1\rho,16}/\sigma_{R1\rho,16} & \cdots & [\vec{r}_5]_{R1\rho,16}/\sigma_{R1\rho,16} \\ [\vec{r}_0]_{R1\rho,25}/\sigma_{R1\rho,25} & [\vec{r}_1]_{R1\rho,25}/\sigma_{R1\rho,25} & \cdots & [\vec{r}_5]_{R1\rho,25}/\sigma_{R1\rho,25} \\ [\vec{r}_0]_{R1\rho,38}/\sigma_{R1\rho,38} & [\vec{r}_1]_{R1\rho,38}/\sigma_{R1\rho,38} & \cdots & [\vec{r}_5]_{R1\rho,38}/\sigma_{R1\rho,38} \\ [\vec{r}_0]_{R1\rho,51}/\sigma_{R1\rho,51} & [\vec{r}_1]_{R1\rho,51}/\sigma_{R1\rho,51} & \cdots & [\vec{r}_5]_{R1\rho,51}/\sigma_{R1\rho,51} \\ [\vec{r}_0]_{R1,400}/\sigma_{R1,400} & [\vec{r}_1]_{R1,400}/\sigma_{R1,400} & \cdots & [\vec{r}_5]_{R1,400}/\sigma_{R1,400} \\ [\vec{r}_0]_{R1,500}/\sigma_{R1,500} & [\vec{r}_1]_{R1,500}/\sigma_{R1,500} & \cdots & [\vec{r}_5]_{R1,500}/\sigma_{R1,500} \\ [\vec{r}_0]_{R1,850}/\sigma_{R1,850} & [\vec{r}_1]_{R1,850}/\sigma_{R1,850} & \cdots & [\vec{r}_5]_{R1,850}/\sigma_{R1,850} \\ [\vec{r}_0]_{S^2}/\sigma_{S^2} & [\vec{r}_1]_{S^2}/\sigma_{S^2} & \cdots & [\vec{r}_5]_{S^2}/\sigma_{S^2} \end{pmatrix} \cdot \begin{pmatrix} \rho_0^{(\theta,S)} \\ \rho_1^{(\theta,S)} \\ \rho_2^{(\theta,S)} \\ \rho_3^{(\theta,S)} \\ \rho_4^{(\theta,S)} \end{pmatrix}, \qquad \text{(S1)}$$

where the $\vec{r}_n$ are given in SI Table I and SI Table II (solved using 'fit_data.m' in the DIFRATE package). Other parameters required for calculating detector sensitivities are also given. Normalized rate constant sensitivities and detectors resulting from the experimental parameters and detection vectors in SI Table I are plotted in SI Fig. 1.

Note that we have previously shown that R_1 and $R_{1\rho}$ are nearly orthogonal in the 'reduced space' of relaxation rate constants (see ref. [1], Fig. 7). Because of this, we can optimize a set of R_1 detectors and, separately, a set of $R_{1\rho}$ detectors for analysis, and later combine with the order parameter, $1–S^2$. This results in block-diagonal matrices in SI Table I and SI Table II. If we do not optimize the detectors separately, very small values replace the zeros, resulting in nearly invisible changes to sensitivities and experimental detector responses. This does not mean that some motion cannot influence both R_1 and $R_{1\rho}$ relaxation, but such a motion in between the sensitive ranges of R_1 and $R_{1\rho}$ would increase both $\rho_2^{(\theta,S)}$ and $\rho_3^{(\theta,S)}$.

SI Table I: Detection vectors and parameters for main text Figs. 1 and 4.

	$\vec{r}_0$	$\vec{r}_1$	$\vec{r}_2$	$\vec{r}_3$	$\vec{r}_4$	$\omega_r/2\pi$ / ms^{-1}	$\omega_1/2\pi$ / ms^{-1}	B_0/T
$R_{1\rho,10}$ / ms^{-1}	0	0	0	2.5493	0.2121	60	10.8	19.96
$R_{1\rho,16}$ / ms^{-1}	0	0	0	2.5611	0.2756	60	16.1	19.96
$R_{1\rho,25}$ / ms^{-1}	0	0	0	2.6253	0.4835	60	24.5	19.96
$R_{1\rho,38}$ / ms^{-1}	0	0	0	1.9951	0.9841	60	37.6	14.09
$R_{1\rho,51}$ / ms^{-1}	0	0	0	1.6584	3.9584	60	50.8	14.09
$R_{1,400}$ / s^{-1}	0	2.2144	3.3930	0	0	–	–	11.74
$R_{1,500}$ / s^{-1}	0	2.3359	2.4975	0	0	–	–	14.09
$R_{1,850}$ / s^{-1}	0	2.6170	1.1230	0	0	–	–	19.96
$1–S^2$	7.5121	0.8419	0.7998	1.0729	0.8285	–	–	–

Other parameters: $\delta_{HN}/2\pi$ = -22283 Hz, $\Delta\sigma_N$ = 169.5 ppm

SI Table II: Detection vectors and parameters for SI Fig. 6 and SI Fig. 7.

	$\vec{r}_0$	$\vec{r}_1$	$\vec{r}_2$	$\vec{r}_3$	$\vec{r}_4$	$\omega_r/2\pi$ / ms^{-1}	$\omega_1/2\pi$ / ms^{-1}	B_0/T
$R_{1\rho,10}$ / ms^{-1}	0	0	0	2.6479	0.2175	60	10.8	19.96
$R_{1\rho,16}$ / ms^{-1}	0	0	0	2.6602	0.2826	60	16.1	19.96
$R_{1\rho,25}$ / ms^{-1}	0	0	0	2.7269	0.4956	60	24.5	19.96
$R_{1\rho,38}$ / ms^{-1}	0	0	0	2.0996	1.0219	60	37.6	14.09
$R_{1\rho,51}$ / ms^{-1}	0	0	0	1.7449	4.1110	60	50.8	14.09
$R_{1,400}$ / s^{-1}	0	2.3419	3.5634	0	0	–	–	11.74
$R_{1,500}$ / s^{-1}	0	2.4616	2.6128	0	0	–	–	14.09
$R_{1,850}$ / s^{-1}	0	2.7218	1.1584	0	0	–	–	19.96
$1–S^2$	7.5208	0.8429	0.7935	1.1090	0.7890	–	–	–

Other parameters: $\delta_{HN}/2\pi$ = -22945 Hz, $\Delta\sigma_N$ = 169.5 ppm

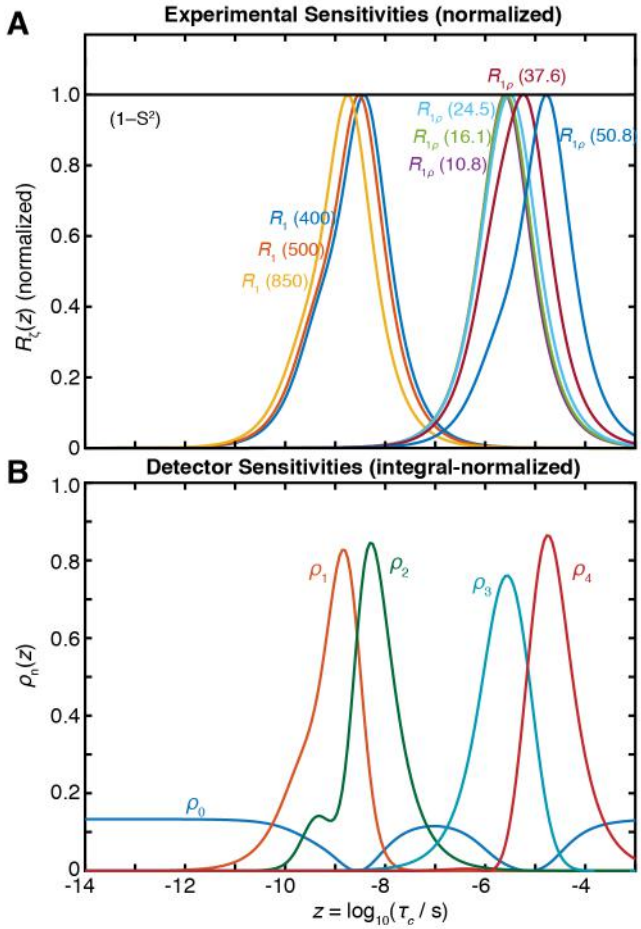

SI Fig. 1. Normalized experimental sensitivities and detector sensitivities. **A** plots the sensitivities of 9 experiments, all normalized to a maximum of 1. R_1 experiments are labeled with the ^{1}H Larmor frequency in MHz, and $R_{1\rho}$ experiments are labeled with the spin-lock strength in kHz. **B** shows linear combinations of those sensitivities, yielding detector sensitivities. Rate constant sensitivities and detector sensitivities are obtained using the parameters in SI Table I.

We also plot the experimental data used for obtaining detector responses, and the fit obtained using detection vectors in SI Table I (detection vectors in SI Table II achieve a near-identical fit- the change in reference bond length mainly scales the detector responses). Note that we simultaneously fit $R_{1\rho}$ data, with results appearing in main text Fig. 4 and SI Fig. 26.

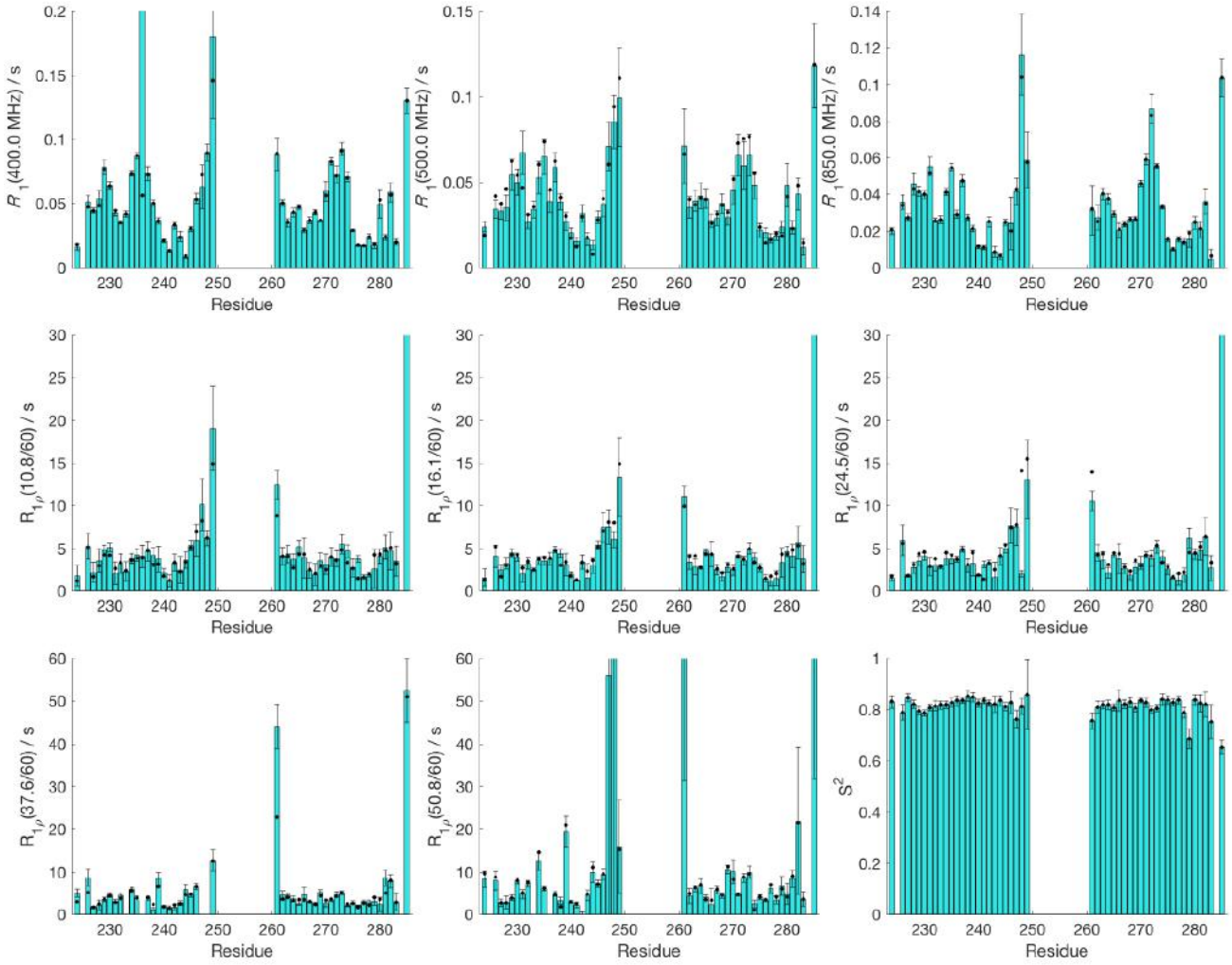

SI Fig. 2. Fit of experimental data, using detection vectors found in SI Table I. Experimental data is taken from reference [3].

1.2. Molecular dynamics setup

Setup of the MD trajectories followed the procedure of Dolenc et al.[4] and Lange et al.[5], using both the GROMOS 54a7[6] and AMBER 99SB-ILDN[7] force fields. The initial atom coordinates were taken from a solid-state NMR structure (PDB ID: 2KJ3).[8] Three HET-s molecules (residues 218-289) were used, while subsequent analysis was performed on the center molecule (cross-correlation is calculated also to the upper and lower molecule).

The simulations using the GROMOS 54a7 force field were performed using the GROMOS software package.[9] The trimer was solvated with 20'559 water molecules in a cubic box with periodic boundary conditions, and the energy minimized with the protein coordinates position restrained (K = 2.5 x 10^4 kJ mol^{-1} nm^{-2}). The system was further thermalized from 60 K to 298 K, in steps of 60 K (60, 120, 180, 240, 298 K), with equilibration for 50 ps at each temperature. The first four steps were carried out under constant volume (NVT), the

last 50 ps at 298 K at constant pressure (NPT). The production run was 250 ns. Newton's equations of motion were integrated using the leapfrog scheme[10] with a time step of 2 fs. The simple-point-charge (SPC) water model[11] was used. To keep the temperature close to its reference value, weak coupling to a temperature bath with a relaxation time of 0.1 ps was applied.[12] The peptides and the solvent were coupled to separate temperature baths. The pressure was maintained close to 1.013 bar (1 atm) by weak coupling to a pressure bath with a relaxation time of 0.5 ps and an isothermal compressibility of 4.575×10^{-4} kJ^{-1} mol^{1} nm^{3}. A twin-range cutoff scheme with 0.8 and 1.4 nm was used for the nonbonded interactions. A reaction field force[13] with a relative dielectric permittivity of 61[14] was applied to treat electrostatic interactions beyond the long-range cutoff. All bond lengths were constrained to ideal values using the SHAKE algorithm[15] with a tolerance of 10^{-4}. The center of mass motion was stopped every 2 ps. The coordinates were written out every 5 ps for analysis.

The simulations using the AMBER 99SB-ILDN force field were performed using the GROMACS 4.5.7 software package.[16] The trimer was solvated with 12'966 water molecules in a cubic box with periodic-boundary conditions, and the energy minimized. Equilibration involved 100 ps at 298 K under NVT conditions, followed by 100 ps at 298 K under NPT conditions. The production run was 500 ns. The integration time step was 2 fs. The TIP3P water model[17] was used. The same thermostat and barostat techniques and parameters were used as for the GROMOS simulations. Separate temperature baths were used for the peptides and the solvent. The particle-mesh Ewald (PME) method[18] with a straight cutoff of 1.0 nm was used for the nonbonded interactions. All bond lengths were constrained to ideal values using the LINCS algorithm[19] with an order of four. The center of mass motion was stopped every 20 fs. The coordinates were written out every 5 ps for analysis.

2. Relating detector responses to order parameters

Detectors are a relatively new concept for the characterization of dynamics, so that the interpretation of a detector response is not immediately obvious. We discuss here briefly the relationship of detector responses to the more traditional order parameter, S^2. In relaxation studies, the *total* order parameter gives the value of the correlation function at time $t = \infty$, for example, the exponentials in main text eq. (1) become zero, such that

$$C(t) = \lim_{t\to\infty}\left[S^2 + (1-S^2)\int_{-\infty}^{\infty} \theta(z)\exp(-t/10^z \cdot 1\,\mathrm{s})\,dz \right] = S^2 \quad \text{(S2)}$$

The order parameter (strictly speaking, $1–S^2$), tells us about the total amount of motion for a given bond, without any dependence on correlation time (experimentally, we will not see some motions with correlation times longer than the timescale of the experiment used to measure the order parameter, but we neglect this in our example here). In other words, $(1-S^2)$ is just the integral of the distribution of motion ($(1-S^2)\theta(z)$ integrates to $(1-S^2)$, since by definition $\theta(z)$ integrates to 1). On the other hand, detector responses depend on a sensitivity, which is a function of correlation time, such that

$$\rho_n^{(\theta,S)} = (1-S^2)\int_{-\infty}^{\infty} \theta(z)\rho_n(z)\,dz \quad \text{(S3)}$$

We plot an example distribution of motion in SI Fig. 2, and the sensitivities of several equal-maximum normalized detectors, $\rho_n(z)$. Note that we can think of the sensitivity of the order parameter as being 1 for all z, since replacing $\rho_n(z)$ in eq. (S3) with 1 results simply in an integral of the distribution. Then, the area under the distribution in SI Fig. 2A is $(1-S^2)$ (region highlighted in grey in SI Fig. 2A). The product of the sensitivity of each detector, $\rho_n(z)$, with the distribution is also plotted in SI Fig. 2A, with the area under each resulting curve highlighted in color. The areas under these curves correspond to the detector responses ($\rho_n^{(\theta,S)}$), where $(1-S^2)$ and the $\rho_n^{(\theta,S)}$ are shown in SI Fig. 2B. Then, we see that each detector selects a part of the total amount of $(1–S^2)$, where that part corresponds to a specific range of correlation times.

Equal-maximum normalized detectors yield the part of $(1-S^2)$ where a detector is sensitive, and so are comparable to traditional order parameters. However, in this study, we eventually conclude that motion is broadly distributed over a wide range of correlation times. In this case, it is possible to estimate the amplitude of the distribution itself at the detector centers, z_n^0, if we use equal-integral normalized detectors (ref. [1], Fig. 11(b), where this relationship is obtained if the distribution is approximately linear over the sensitive range of the detector). We demonstrate this behavior here (SI Fig. 2C), where bars show the detector responses, plotted at the detector center. Then, we see that the bars approximately intersect the distribution. Note that equal-integral normalized detectors yield a weighted average of $(1-S^2)\theta(z)$, where weighting is largest near z_n^0.

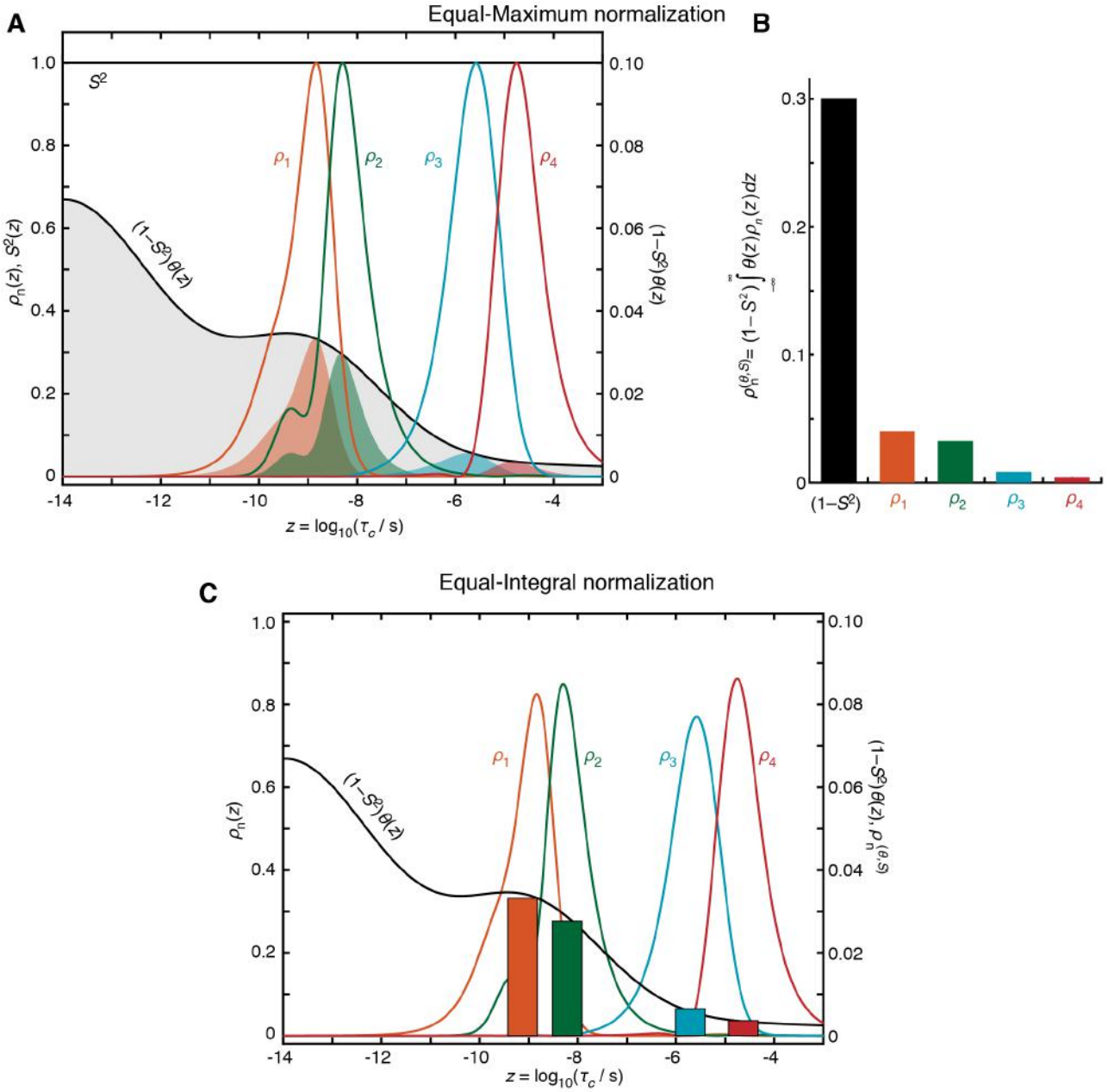

SI Fig. 3. Distribution of motion vs. detector responses. **A** plots the sensitivity of an S^2 measurement and the sensitivities of equal-maximum normalized detectors ρ_1–ρ_4 (left axis). On the right axis, an example distribution of motion is plotted, $(1-S^2)\theta(z)$, and regions highlighted in color correspond to curves obtained from multiplying the distribution by the detector sensitivity, $\rho_n(z)$. The area under these curves is the detector response (or order parameter), which are shown in **B**. We see that each detector response is simply part of the total order parameter, filtered for a specific range of correlation times. **C** shows sensitivities of equal-integral normalized detectors (left axis), and the same distribution of motion. In this case, detector responses (bars, right axis) estimate the amplitude of the distribution of motion (right axis) at the center of the detector, z_n^0.

Equal-integral normalized detectors may also be related to order parameters. However, since these estimate the amplitude of the distribution, we must define a range of

correlation times for which we are interested. For example, in main text Fig. 1, we see that for residue 235E, the average of $\rho_1^{(\theta,S)}$ and $\rho_2^{(\theta,S)}$ is 0.015. These two detectors are separated by about an order of magnitude, so we could estimate that the distribution of motion has an average amplitude of approximately $\left\langle (1-S^2)\theta(z)\right\rangle \approx 0.015$ over a range $\Delta z = 1$. Then, we can estimate that $(1-S_i^2)$, i.e. an order parameter for the part of the total motion in this region, is given by $(1-S_i^2) = \left\langle (1-S^2)\theta(z)\right\rangle \Delta z = 0.015 \times 1 = 0.015$. However, we do not know if the actual motion covers a broader range of correlation times than this (MD suggests it may cover ~2.5 orders of magnitude, see SI Fig. 13). If we take this broader range, then we arrive at $(1-S_i^2) = 0.015 \times 2.5 = 0.037$. Due to the uncertainty in the range, Δz, that a given motion may cover, we prefer to simply report the detector response, $\rho_n^{(\theta,S)}$, directly, although this approximation is still useful to obtain a more familiar representation of the internal dynamics.

3. Calculating detector responses from MD

3.1. Calculating the correlation function

Relaxation due to re-orientational motion in NMR is a function of the time-correlation function of rank-2 tensors. If we consider motion of some bond vector with index *k*, given by a time-dependent unit vector, $\mathbf{e}_k(\tau)$, we can calculate the correlation function for the rank-2 tensor aligned with that bond vector (for example, representing the dipole coupling tensor between the two nuclei connected by that bond, in this study the backbone ^{1}H and ^{15}N nuclei).

$$C(t) = \left\langle P_2(\mathbf{e}_k(\tau)\cdot\mathbf{e}_k(t+\tau))\right\rangle_\tau \qquad \text{(S4)}$$

Here, $P_2(x) = (3x^2-1)/2$, the second Legendre polynomial, where we take the dot product between the bond vector at times τ and $t+\tau$. This yields the cosine of the angle between the two vectors (since $\mathbf{e}_k(\tau)$ is normalized to a length of one). This value is averaged over the initial time, τ. Numerically, Eq. (S2) is calculated from a trajectory as

$$C(t_n) = \frac{1}{N-n}\sum_{i=0}^{N-n-1}\frac{1}{2}\left(3((\mathbf{e}_k(t_i)\cdot\mathbf{e}_k(t_{i+n}))^2-1)\right), \qquad \text{(S5)}$$

where the time points in the MD trajectory are indexed from 0 to *N*–1 (for *N* time points).[20] For the n^{th} time point of the correlation function, we take an average over *N*–*n* pairs of time points (for the n^{th} time point, we average over all time points in the trajectory separated by

n, so the first pair of time points is *i*=0 and *i*=*n*, and the last pair of time points is *i*=*N*–*n*–1 and *i*=*N*–*1*, which gives *N*–*n* pairs of time points in total). Note that before calculating the correlation function, we remove overall motion by superposition of the solute center-of-mass and by aligning the Cα of the middle HET-s molecule for residues 226-245 and 262-281 to a reference HET-s(218-289) structure, following the procedure of Dolenc et al.[4]

3.2. Inverse Laplace transforms

We assume that for each H–N bond, the correlation function extracted from the MD trajectory can be constructed from a sum of decaying exponential terms,[1] such that the correlation function is given by a distribution of correlation times:

$$C(t_n) = S^2 + (1-S^2)\int_{-\infty}^{\infty} \theta(z)\exp(-t/(10^z \cdot 1\,\mathrm{s}))dz \qquad \text{(S6)}$$

Then, we may fit the correlation functions calculated from Eq. (S5) to a discretized version of Eq. (S6), given as

$$C(t_n) = S^2 + \sum_{m=1}^{M} [\vec{\theta}]_m \exp(-t_n/(10^{z_m} \cdot 1\,\mathrm{s})) \qquad \text{(S7)}$$

,

where $\vec{\theta}$ is a discretized form of the distribution (we absorb the prefactor, 1–S^2, into the discretized distribution, $\vec{\theta}$). To fit this function, we first construct a matrix, **M**:

$$\mathbf{M} = \begin{pmatrix} \exp(-t_0/10^{z_1}) & \exp(-t_0/10^{z_2}) & \cdots & \exp(-t_0/10^{z_M}) \\ \exp(-t_1/10^{z_1}) & \exp(-t_1/10^{z_2}) & \cdots & \exp(-t_1/10^{z_M}) \\ \vdots & \vdots & \ddots & \vdots \\ \exp(-t_{N-1}/10^{z_1}) & \exp(-t_{N-1}/10^{z_2}) & \cdots & \exp(-t_{N-1}/10^{z_M}) \end{pmatrix} \qquad \text{(S8)}$$

The *z* that run across each row yield the correlation times included in the fit ($\tau_m = 10^{z_m} \cdot 1\,\mathrm{s}$), where we use *M* = 200 correlation times logarithmically spaced between 10 fs and 1 ms (note, we cannot reasonably extract 1 ms correlation times from a 500 ns trajectory, but we include rather long correlation times instead of trying to estimate where best to cut off the distribution). The different time points, t_n, run down each column.

Then, we can construct a vector, $\vec{C}$, which contains all numerically calculated values of $C(t_n)$ for some H–N bond, and solve

$$\vec{C} = \mathbf{M} \cdot \vec{\theta} + \vec{\epsilon}\,, \qquad \text{(S9)}$$

$\vec{\epsilon}$ is a vector containing the error of the fit of the distribution to the correlation function. We minimize $\vec{w} \cdot |\vec{\epsilon}|^2$, which is the sum of squares of the error, $|\vec{\epsilon}|^2$, times a weighting factor, $\vec{w}$. Here, $\vec{\theta}$ is the discretized form of the distribution function, $(1-S^2)\theta(z)$ (where 1–S^2 is

included in $\vec{\theta}$). The exponential terms with the longest correlation times (up to 1 ms) result in essentially flat functions for our 250 and 500 ns trajectories. Then, we can omit S^2 from Eqs. (S8) and (S9), and the offset due to S^2 is easily absorbed into the longest correlation times.

Note that if we minimize the 2-norm of $\vec{\epsilon}$ directly, we will prioritize the fitting of longer timescales, for example, ns vs. ps, since there are more time points fitted for the longer correlation times. Therefore, we re-weight the fit and minimize

$$\vec{w}\cdot|\vec{\epsilon}|^2=\sum_{n=0}^{N-1}(\log(t_{n+1})-\log(t_n))\left(C(t_n)-[\mathbf{M}\cdot\vec{\theta}]_n\right)^2, \tag{S10}$$

so that all decades will be equally well-fit ($w_n=(\log(t_{n+1})-\log(t_n))$). For n = 0 (t_0 = 0 s, $C(t_0)$ = 1), this adds infinite weighting; in fact, we would like a perfect fit of the first time point, but numerically using infinite weighting is not possible. Thus, we set the weighting of the t_0 equal to the weighting of t_1, and after fitting, we correct fitting of $C(t_0)$ = 1, by setting $[\vec{\theta}]_1=1-\sum_{m=2}^{M}[\vec{\theta}]_m$, so that the sum of the discretized distribution is exactly one (usually this adjustment is negligible). Note that we resolve another problem with this weighting scheme: the correlation function is badly estimated by Eq. (S5) for long correlation times, since only a few time points are included in the average. Log-weighting gives low priority to the fitting of these time points, so that noise at these points does not affect the fit quality significantly (an alternative approach to resolve this issue is to simply truncate the correlation function to be shorter than the trajectory length, although it is somewhat arbitrary where to truncate the trajectory). The weighting of the last time point is undefined (t_{N-1}), so we set the weighting for t_{N-1} equal to the weighting of t_{N-2}.

A problem remains, in that we allow very long correlation times in the distribution, $\vec{\theta}$, but in principle cannot characterize these accurately. We could cut the distribution off at some correlation time, but the location of this cutoff is also somewhat arbitrary. Therefore, we note that it is possible to calculate the total order parameter, S^2, assuming that the trajectory samples all configurations (with the correct weighting of those configurations). This is calculated as

$$S^2=\frac{3}{2}\left[\sum_{\alpha=1}^{3}\sum_{\beta=1}^{3}\left\langle[\mathbf{e}_k(\tau)]_\alpha[\mathbf{e}_k(\tau)]_\beta\right\rangle_\tau^2\right]-\frac{1}{2}, \tag{S11}$$

where the indices α,β = 1-3 indicate the x, y, and z directions (derived in [21], see Eqs. 8 and 11b, where $C(t\rightarrow\infty)$ is calculated, note that in the reference, $C(t)$ is scaled by the NMR

interaction size, whereas the interaction size is not included here). Then, we force the fitted correlation function to have a final value of S^2, by requiring that

$$\sum_{m=1}^{M}[\vec{\theta}]_m = 1 - S^2 . \qquad \text{(S12)}$$

This is achieved by progressively removing amplitude from the $[\vec{\theta}]_m$ starting from the longest correlations and moving towards shorter correlation times, until Eq. (S12) is satisfied.

This approach gives a stable value for the end of the correlation function $(C(t \to \infty) = S^2)$, whereas otherwise we must rely on the values determined for long correlation times with Eq. (S5), which are extremely unstable (see SI Fig. 4 and SI Fig. 5 for example). Furthermore, we are not required to select an arbitrary cutoff for the longest correlation times allowed in the distribution. Note that the assumption that the trajectory samples all configurations is not usually correct, but as long as the calculated detectors do not depend strongly on correlation times significantly longer than the trajectory, this will not strongly influence our calculation. An exception arises if a slow motion that is not fully sampled results in a reconfiguration of the protein that significantly modifies the faster dynamics; in this case, the lack of sampling will influence the characterization of the faster motions. Fits of the correlation functions obtained using AMBER and GROMOS force fields are shown in SI Fig. 4 and SI Fig. 5, respectively. Note that the ends of the correlation functions are not well fit, due to the weighting in Eq. (S10), but are forced to level off at the value of S^2 calculated in Eq. (S11).

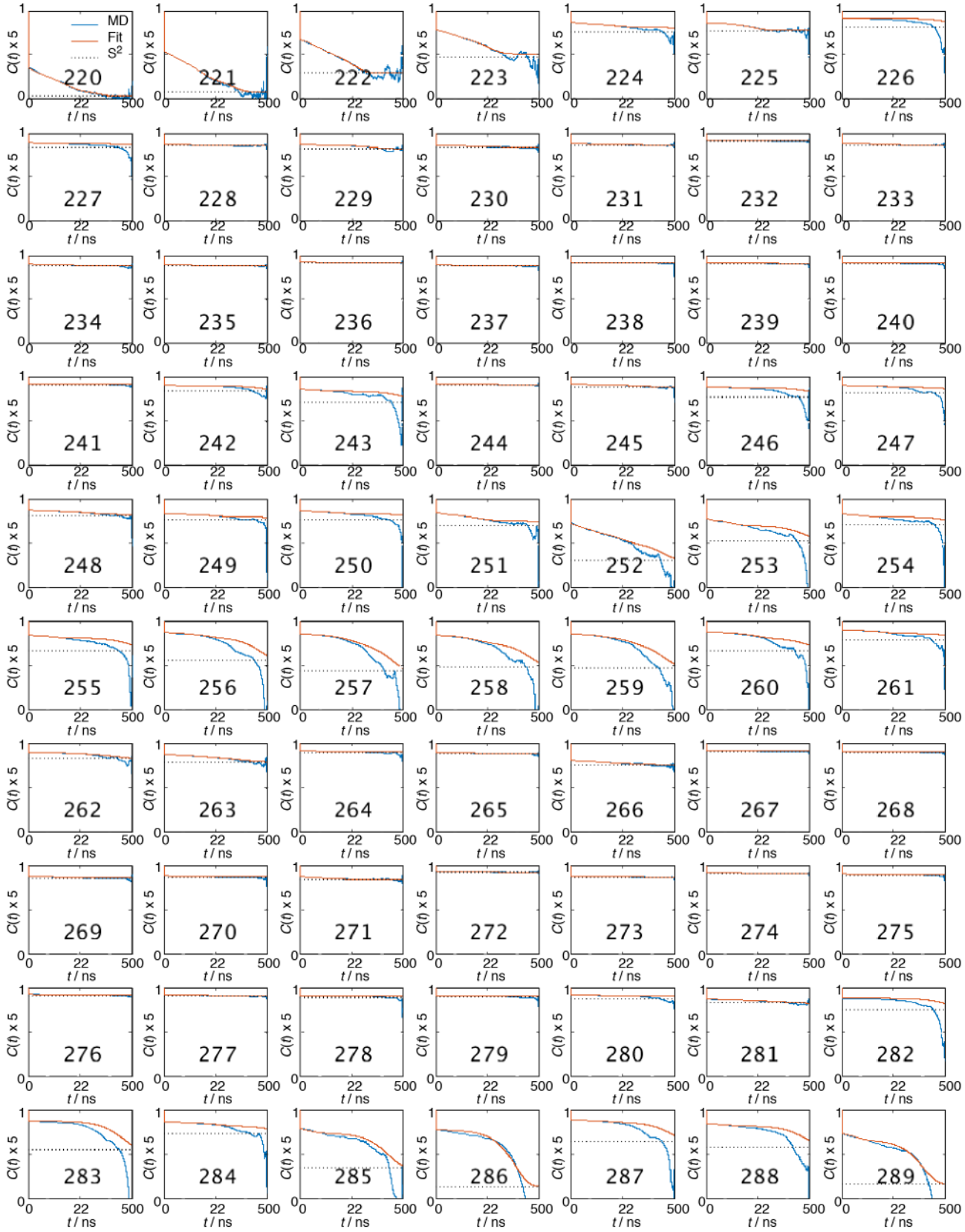

SI Fig. 4. Fits for inverse Laplace transform for the AMBER 99SB-ILDN force field. MD derived correlation functions shown in blue, and fit in red. Residue number is indicated in each plot. x-axis is on a log scale, although the t = 0 s point is shown, placed at the same x-axis position as the second time point (t = 5 ps). Fits are forced to level off at S^2 (Eq. (S11)), which is indicated with a dotted line in each plot.

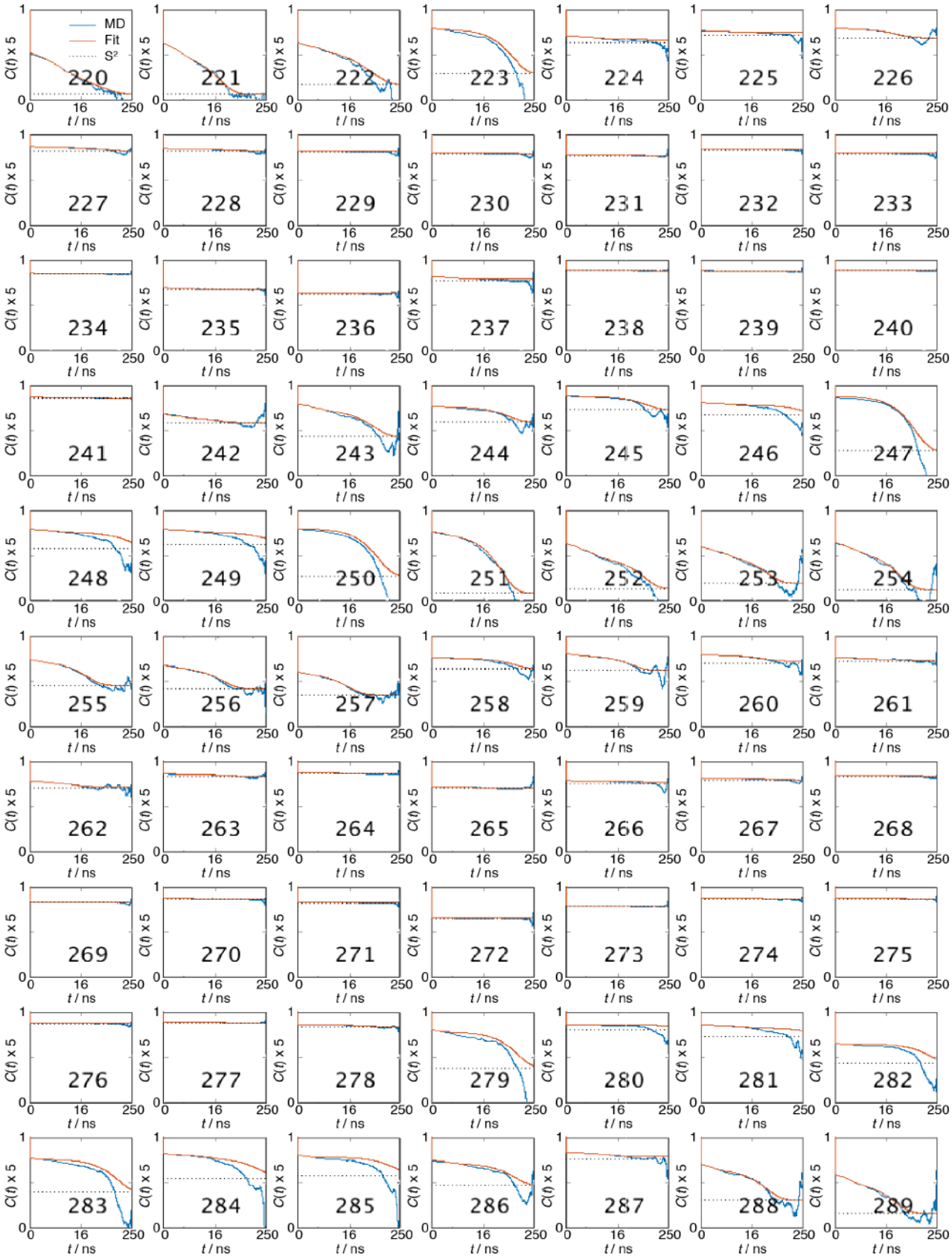

SI Fig. 5. Fits for inverse Laplace transform for the GROMOS 54a7 force field. MD derived correlation functions shown in blue, and fit in red. Residue number is indicated in each plot. x-axis is on a log scale, although the t = 0 s point is shown, placed at the same x-axis position as the second time point (t = 5 ps). Fits are forced to level off at S^2 (Eq. (S11)), which is indicated with a dotted line in each plot.

We should note a few practical aspects of fitting. We use the 'lsqlin.m' function in MATLAB to solve Eq. (S10), where we enforce that all elements of $\vec{\theta}$ are non-negative. Then, the elements of the discretized distribution, $\vec{\theta}$, are related to the continuous distribution, $(1-S^2)\theta(z)$, according to

$$[\vec{\theta}]_m \approx (1-S^2)\theta(z_m)\Delta z\,. \tag{S13}$$

where Δz is the spacing between the log of the correlation times ($\Delta z = z_{m+1} - z_m$ for all m). Discretization leads to small errors, so we indicate this throughout ($\approx$), although typically errors from the approximation are negligible.

3.3. Numerical calculation of detector responses and relaxation-rate constants

Detector responses may be calculated from the discretized distribution function, $\vec{\theta}$, according to

$$\rho_n^{(\theta,S)} = (1-S^2)\int_{-\infty}^{\infty}\theta(z)\rho_n(z)dz \approx \sum_{m=1}^{M}[\vec{\theta}]_m\rho_n(z_m)\,. \tag{S14}$$

Eqs. (S7) and (S13) show that dz and $(1–S^2)$ are absorbed into $[\vec{\theta}]_m$ in the discretized form. One may similarly calculate relaxation-rate constants directly, using the same approach, and simply replacing the detector sensitivity with the relaxation rate constant sensitivity.

$$R_\zeta^{(\theta,S)} = (1-S^2)\int_{-\infty}^{\infty}\theta(z)R_\zeta(z)dz \approx \sum_{m=1}^{M}[\vec{\theta}]_m R_\zeta(z_m)\,. \tag{S15}$$

Note that the rate constant sensitivity, $R_\zeta(z)$, is defined as the rate constant obtained for motion having a single correlation time $\tau = 10^z \cdot 1\,\mathrm{s}$ and an forder parameter such that $1-S^2 = 1$.[1] Detector responses calculated using Eq. (S14) are shown for the AMBER force field in the main text, Fig. 1, and for the GROMOS force field in SI Fig. 7. Relaxation-rate constants are discussed in SI section 4.1, with MD results shown in SI Fig. 9 and SI Fig. 10.

3.4. Additional detector-response calculations

In the main text, Fig. 1, we calculate experimental detector responses using a reference bond length of 1.03 Å, which is longer than the more often used 1.02 Å.[22] While 1.03 Å yields better agreement between ρ_0 detectors calculated from MD using the AMBER 99SB-ILDN force field and the experimentally determined detectors, we also compare using 1.02 Å, shown in SI Fig. 6. Using a shorter bond length, in effect, means that more fast motions are included in the detector response, $\rho_0^{(\theta,S)}$ (primarily vibrational and librational

motions). We see here that use of a shorter bond length when analyzing experimental data results in higher amplitude $\rho_0^{(\theta,S)}$ responses than found with the AMBER trajectory.

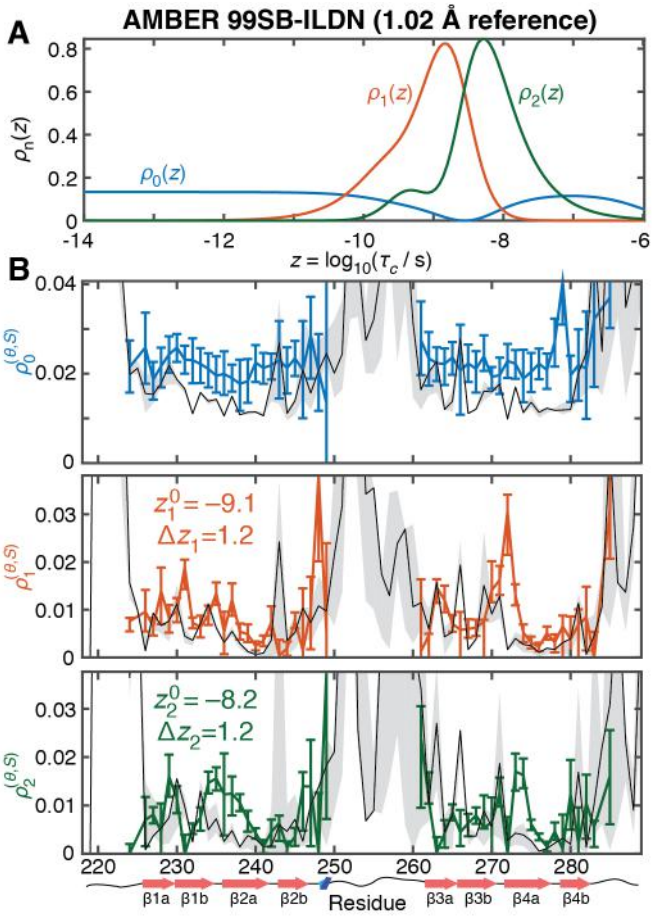

SI Fig. 6. Comparison of NMR detector analysis with a reference bond length of 1.02 Å and detector responses calculated from a 500 ns AMBER 99SB-ILDN MD trajectory. **A** shows the sensitivities, $\rho_n(z)$ of the three detectors. **B** shows the response of the three detectors as determined via NMR (colored lines, error bars give 95% confidence interval), and via MD simulation (black lines). The grey region is an approximate confidence interval for MD results, obtained by analyzing the first and second halves of the trajectory separately, and plotting the range of results.

We can understand this discrepancy in part by investigating the literature carefully to understand the origin of the 1.02 Å reference bond length. In fact, 1.041 Å is also proposed as a reference length. David Case suggests this length, based on theoretical calculation of the average bond length using $1/r^6$ averaging (since effective relaxation rates are affected by this term), for the H–N bond of N-methylacetamide in water at 0 K.[23] Using this reference length, resulting order parameters (where $1–S^2$ relates the amplitude of motion) or in our case, detector responses in principle exclude all ground state (0 K) motion, and only include motion appearing as the temperature is raised to room temperature. This result is consistent with experimental NMR measurements of Ottiger and Bax in aligned media.[24] However, Bernado and Blackledge later show that some of the excluded H–N motions are asymmetric, especially those resulting from peptide plane motion, so that while the average length of 1.041 Å may be correct, it actually corresponds to an asymmetric dipolar

tensor.[22] 1.02 Å is proposed as a reference length so that these asymmetric peptide plane motions are included in the dynamics analysis rather than removed via the average bond length. As such, we expect that using a 1.02 Å reference length then includes some of the ground-state vibrational motions in resulting values of $1–S^2$ or $\rho_0^{(\theta,S)}$.

These results, however, make it unclear how to compare the resulting values of $\rho_0^{(\theta,S)}$ (or $1–S^2$) to results obtained from MD. MD is a classical method, and so strictly speaking, has no true "ground state" vibrational motions since these are a quantum mechanical effect. However, to accurately reproduce protein dynamics, similar vibrations/librations are produced by the simulation, although not necessarily with the same amplitude as is present in the quantum-mechanical motion. In the absence of a clearly 'correct' reference bond length, we have optimized the reference bond length to give the best overall agreement between the experimental and simulated values of $\rho_0^{(\theta,S)}$, arriving at a reference length of 1.03 Å. We expect this length to change depending on force field (for example, see SI Fig. 7 where we use 1.02 Å for comparison to the GROMOS force field). We note that this means that we should not over-interpret the good agreement of the average values of NMR- and MD-derived $\rho_0^{(\theta,S)}$ values, however, similar trends observed in main text Fig. 1 is indicative of good performance of the MD simulation.

For further investigation, we have also compared experimental detector responses using a second force field, GROMOS 54a7. In this case, a reference bond length of 1.02 Å yields better agreement between ρ_0 derived with simulation and with experiment, as shown in SI Fig. 7. Agreement of detectors ρ_1 and ρ_2 is worse with the GROMOS force field. In particular, a number of residues show significantly more motion in simulation than experiment (e.g. for ρ_0: 235-236, 243-244, 272; for ρ_1: 242, 262, 279; for ρ_2: 241-245, 247, 262, 279). For this reason, we show subsequent analysis using the AMBER force-field in the main text, and analysis of the GROMOS force-field in the supporting information.

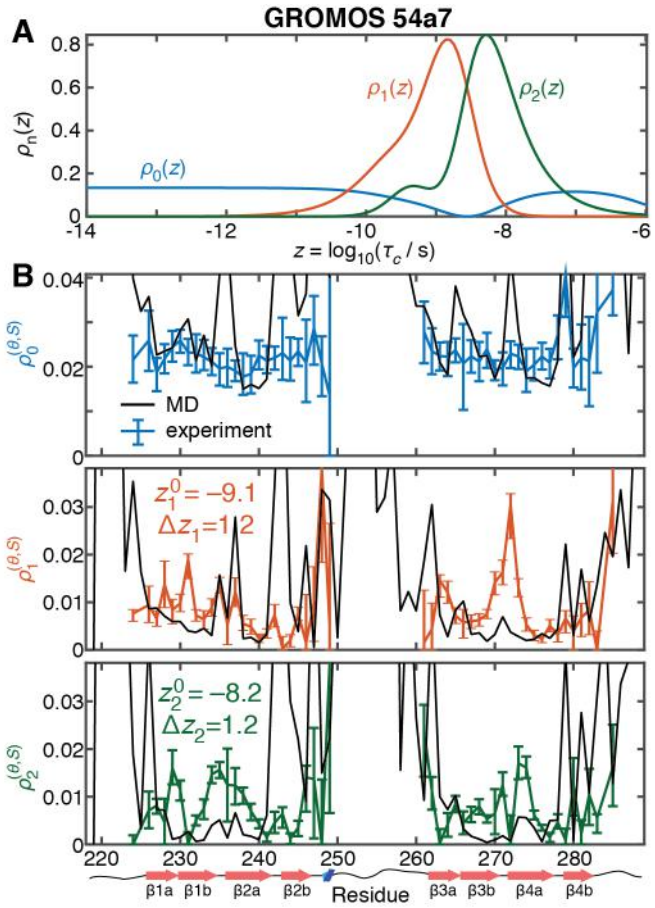

SI Fig. 7. Comparison of NMR detector analysis and detector responses calculated from a 250 ns GROMOS 54a7 MD trajectory. **A** shows the sensitivities, $\rho_n(z)$ of the three detectors. **B** shows the response of the three detectors as determined via NMR (colored lines, error bars give 95% confidence interval), and via MD simulation (black lines).

3.5. Ill-posed problems in the detector analysis

So far, we have neglected the fact that solving Eq. (S10) requires an inverse-Laplace transform, and therefore is a well-known ill-posed problem, meaning that there are multiple solutions.[25] A common approach to solve ill-posed problems is to minimize one of the derivatives of $\vec{\theta}$ (regularization), to force the distribution to be smoother, while still obtaining a high-quality fit of the corresponding correlation function. Note that the regularized solution is not always the correct solution. Instead, one should interpret broadening of the distribution as uncertainty. We show here that although regularization changes the resulting distribution, $\vec{\theta}$, it has little influence on the resulting detector responses. Thus, while we must solve an ill-posed problem to obtain detector responses, the responses themselves are well-defined.

To apply regularization to the calculation of the inverse Laplace transform, while fitting the correlation function of each H–N bond by minimizing Eq. (S10), we simultaneously minimize

$$\lambda \sum_{m=1}^{M-1} \left([\vec{\theta}]_{m+1} - [\vec{\theta}]_m \right)^2 . \qquad \text{(S16)}$$

This has the effect of minimizing the first derivative of $\vec{\theta}$, where the relative priority of minimizing Eq. (S10) and Eq. (S16) is determined by the regularization parameter, λ.[26] By increasing λ, we can change the fits from very narrow distributions to very broad distributions. In SI Fig. 8A, we vary λ, and sum the resulting error in Eq. (S10) over the $C(t)$ for all backbone H–N bonds, so that we see that good fits are obtained until $\lambda > 10^{3.9}$, at which point the distribution functions, $\vec{\theta}$, are forced to be too broad to obtain a good fit. We can see the effect of the regularization parameter for residue 271Gly in SI Fig. 8B, where both distributions yield a good fit of the correlation function. Although these distributions appear to be rather different (two distributions with the same integral, but one with narrow, high intensity lines, and the other with broad, low intensity features), the overlap of the detector sensitivities ($\rho_n(z)$) and the two distributions are about the same, so that Eq. (S14) yields approximately the same values for both distributions. This is shown in SI Fig. 8C, where detector responses for all residues are calculated, using distributions that are fitted with $\lambda = 0$ and $\lambda = 10^{3.9}$. Then, as long as we obtain a good fit of the correlation function, we obtain very similar detector responses for the two values of λ. Note that this will not be the case if detector sensitivities are sufficiently narrow, since the use of regularization may then change the overlap of the distribution and detector sensitivity; practically, we require for the comparison that MD yields a more precise characterization of the correlation times than the experimental detectors (although we do not provide a means for determining that precision here, aside from the test we have just performed). Since detector responses do not change significantly as a function of λ, we simply set $\lambda = 0$ for detector responses and rate constant calculations (Fig. 1B, SI Fig. 6, SI Fig. 7, SI Fig. 9, SI Fig. 10).

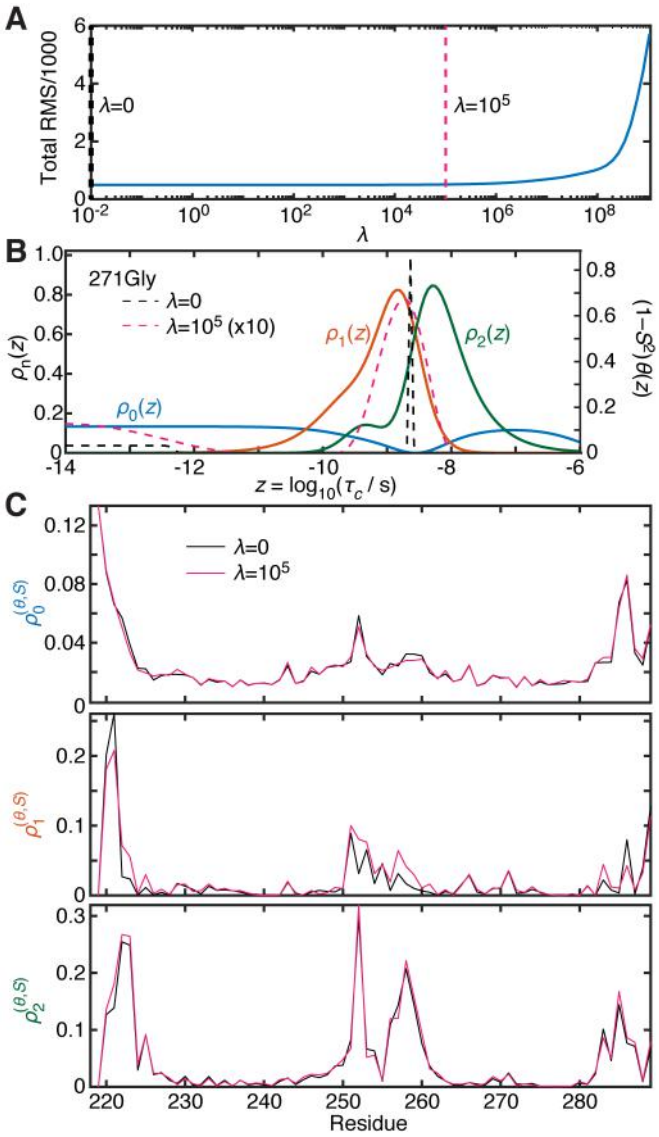

SI Fig. 8. Comparison of results as a function of regularization settings. The inverse Laplace transform is performed for different regularization settings (λ, see SI Eq. (S16)). **A** shows the total RMS for fitting correlation functions of all residues to text Eq. (2) where the regularization parameter is increased from 10^{-2} to 10^{9}. **B** shows the sensitivity ($\rho_n(z)$, solid lines, left axis) of three detectors obtained from NMR data, overlapped with the motional distribution ($(1–S^2)\theta(z)$, dotted lines, right axis), obtained without regularization (black) and with $\lambda=10^{3.9}$ (pink). **C** shows the detector responses calculated from MD without regularization (black lines), and with regularization (pink lines).

4. Fitting to multi-exponential correlation functions

To show the problems arising from analysis of NMR data via fitting to a multi-exponential correlation function (multi-exponential fitting, MEF) for comparison to an MD trajectory, we first calculate relaxation-rate constants from the MD trajectory. We would like to show that poor MEF agreement is a result of the fitting method itself, as opposed to poor performance of the MD simulation. If rate constants are well reproduced compared to experiments, we can show that disagreement in MEF analysis comes primarily from the MEF model itself.

4.1. Rate constants calculated from MD trajectories

We can calculate relaxation-rate constants directly from the MD trajectory, to determine if poor reproduction of rate constants results in disagreement when using the MEF approach. This is usually achieved by fitting MD derived correlation functions to a multi-exponential model of the correlation function, and using the resulting correlation times and amplitudes to calculate contributions to the relaxation rate constants (Eq. (S15)). We implement this using a linear approach, where we allow for 200 different correlation times (log-spaced between 10 fs and 1 ms (the correlation times are fixed, but amplitudes are variable, see section 3.2 and 3.3). An alternative approach is to allow for only a few correlation times, but fit by allowing both the correlation times and amplitudes to vary.[20a, 27] The accuracy of the calculated rates constants should be similar with both methods, as long as a good fit of the correlation function is obtained, although in our hands the linear approach with fixed correlation times is computationally much faster.

The results of calculating R_1 relaxation rate constants from MD trajectories are shown in SI Fig. 9 and SI Fig. 10 for AMBER and GROMOS force fields, respectively. Results of the AMBER force field are generally quite good, with the exception of some underestimation of the relaxation rate constants near β-sheets β2a and β4a. The GROMOS force field yields less agreement, so that we will use the results from the AMBER trajectory to compare model-free analysis of NMR data and MD data.

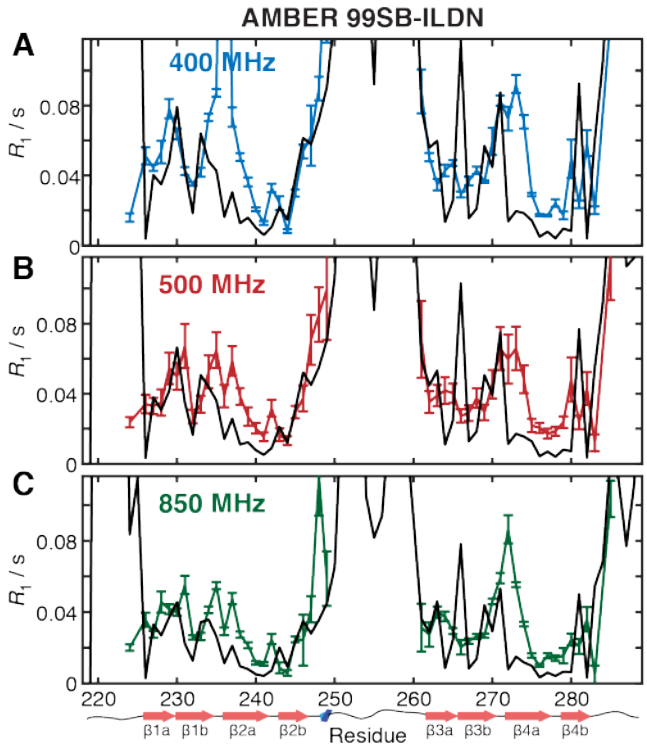

SI Fig. 9. Comparison of ^{15}N R_1 rate constants obtained via NMR experiments and calculated from MD with the AMBER 99SB-ILDN force field. NMR experiments are described in [3]. **A** R_1 at 400 MHz, **B** R_1 at 500 MHz, **C** R_1 at 850 MHz. Colored lines show experimental data with error bars indicating one standard deviation, and black lines show rate constants calculated from MD simulation.

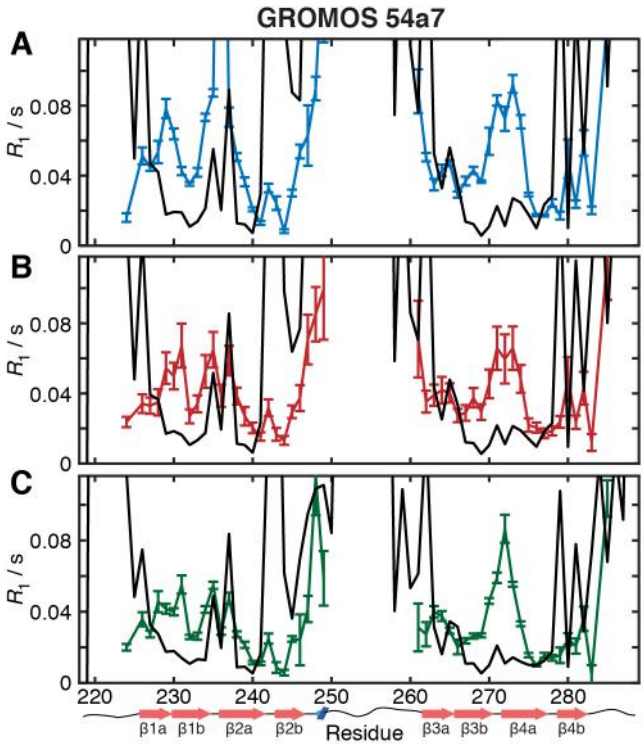

SI Fig. 10. Comparison of ^{15}N R_1 rate constants obtained via NMR experiments and calculated from MD using the GROMOS 54a7. NMR experiments are described in [3]. **A** R_1 at 400 MHz, **B** R_1 at 500 MHz, **C** R_1 at 850 MHz. Colored lines show experimental data with error bars indicating one standard deviation, and black lines show rate constants calculated from MD simulation.

4.2. Fitting MD to a two-correlation time model

Given the good agreement between R_1 rate constants derived with the AMBER force field and measured experimentally, we will now compare multi-exponential fitting (MEF) results of the experimental data and simulation. Previous experimental analysis fitted data (3 R_1, 5 $R_{1\rho}$, and 1 REDOR experiment, to obtain S^2) to a correlation function having three decaying exponential terms.[3] The longest correlation time in the previous study was fitted globally to a value of 6.2 μs. Our trajectory (AMBER) is 500 ns long, so we cannot extract this longest correlation time. Thus, for comparison to MD results, we fit the MD-derived correlation functions to a bi-exponential correlation function with the following form:

$$C(t) = S_f^2 S_i^2 + (1 - S_f^2)\exp(-t/\tau_f) + S_f^2(1 - S_i^2)\exp(-t/\tau_i). \qquad \text{(S17)}$$

We do a simple error minimization between Eq. (S17) and the MD-derived correlation function (Eq. (S5)) for each HN bond in the middle HET-s(218-289) molecule, by varying S_f, S_i, τ_f, and τ_i. Results are shown in SI Fig. 11, and compared to the previously published experimental analysis (the third motion determined experimentally, with τ = 6.2 μs is not shown, since this motion is not compared to the MD results).

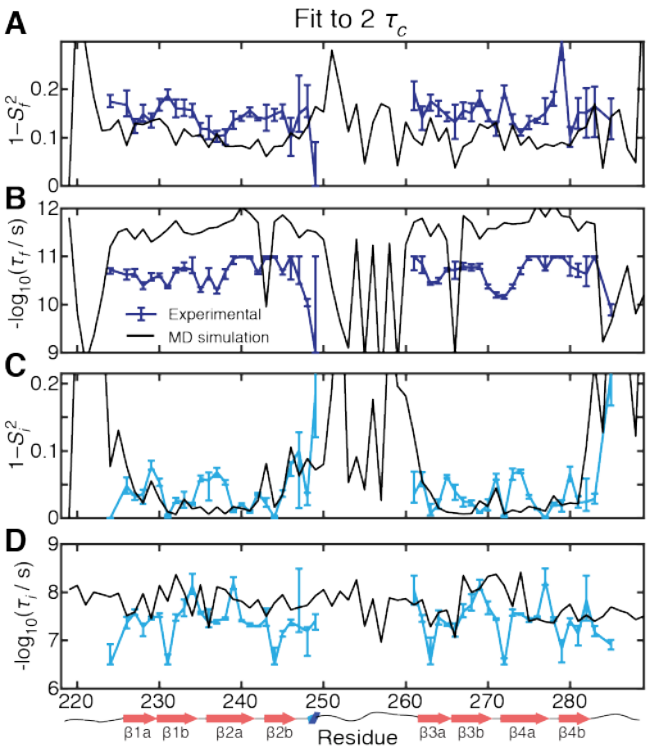

SI Fig. 11. Comparison of MEF results using NMR data fits from ref. [3] and MD data fitted according to Eq. (S17). **A** compares $(1-S_f^2)$ obtained via fitting NMR and MD data. **B** compares τ_f, **C** compares $(1-S_s^2)$, and **D** compares τ_i. In each subplot, colored lines give the experimentally determine parameter, with error bars showing the 68% confidence interval, and black lines show the parameters obtained from fitting to a correlation function obtained from MD. Experimental $R_{1\rho}$ data was fit with a third exponential term, $(1-S_s^2)\exp(-t/\tau_s)$,[3] but is not shown here since the MD trajectory is not long enough for comparison (500 ns, with AMBER 99SB-ILDN force field).

Given the agreement obtained when comparing experimental and simulated R_1 relaxation-rate constants, the disagreement of the MEF-derived parameters is surprising. A large systematic offset is found for τ_f (SI Fig. 11B), and a smaller systematic offset for τ_i (SI Fig. 11D). Amplitude trends for $1-S_i$ are missing, especially around residues 235 and 271 (SI Fig. 11C). If these results were accompanied by poor reproduction of the R_1 rate constants (SI Fig. 9) and poor agreement of the detector responses (main text, Fig. 1), we would assume that the MD does not reproduce the true dynamics well. However, R_1 and detector agreement indicates good MD performance, so that disagreement must be attributed distortions introduced by fitting to a multi-exponential correlation function (or, similarly, by using an oversimplified model to fit the MD-derived correlation functions).

4.3. Fitting MD to a three-correlation time model

A possible source of disagreement between MEF analysis of experimental data and MD-derived correlation functions would be under-fitting of the MD-derived correlation functions. We can reasonably fit a third correlation time to the MD correlation functions such that

$$C(t) = S_1^2 S_2^2 S_3^2 + (1 - S_1^2)\exp(-t/\tau_1) + S_1^2(1 - S_2^2)\exp(-t/\tau_2) + S_1^2 S_2^2(1 - S_3^2)\exp(-t/\tau_3) \quad \text{(S18)}$$

In the Lipari-Szabo model-free approach,[28] all motions falling within the extreme narrowing limit ($\omega\tau$ << 1, for all ω sampled by the experimental data set) are averaged together when fitting NMR relaxation data. For example, if $\omega\tau_1$ << 1 and $\omega\tau_2$ << 1, then the NMR relaxation data will be well-fit with the following correlation function

$$C(t) = S_f^2 S_i^2 + (1 - S_f^2)\exp(-t/\tau_f) + S_f^2(1 - S_i^2)\exp(-t/\tau_i), \quad \text{(S19)}$$

where the terms are given by

$$\begin{aligned} 1 - S_f^2 &= (1 - S_1^2) + S_1^2(1 - S_2^2) \\ \tau_f &= \frac{(1 - S_1^2)\tau_1 + S_1^2(1 - S_2^2)\tau_2}{1 - S_1^2 S_2^2}, \\ S_i^2 &= S_2^2 \\ \tau_i &= \tau_2 \end{aligned} \quad \text{(S20)}$$

Here, the amplitude contributions of $(1 - S_1^2)$ and $S_1^2(1 - S_2^2)$ are simply summed together, and τ_f is the weighted average of τ_1 and τ_2. In SI Fig. 12, the MD correlation function is fitted to Eq. (S18), and compared to the parameters determined from NMR relaxation data, where results for the S_1, S_2, S_3 and τ_1, τ_2, τ_3 are used to calculate S_f, S_i, τ_f, and τ_i according to Eq. (S20). We find much better agreement between τ_f determined via NMR and via MD, however, trends observed for $1–S_i^2$ in the NMR analysis still do not appear in the analysis of the MD trajectory, and systematic offsets of τ_i are still present.

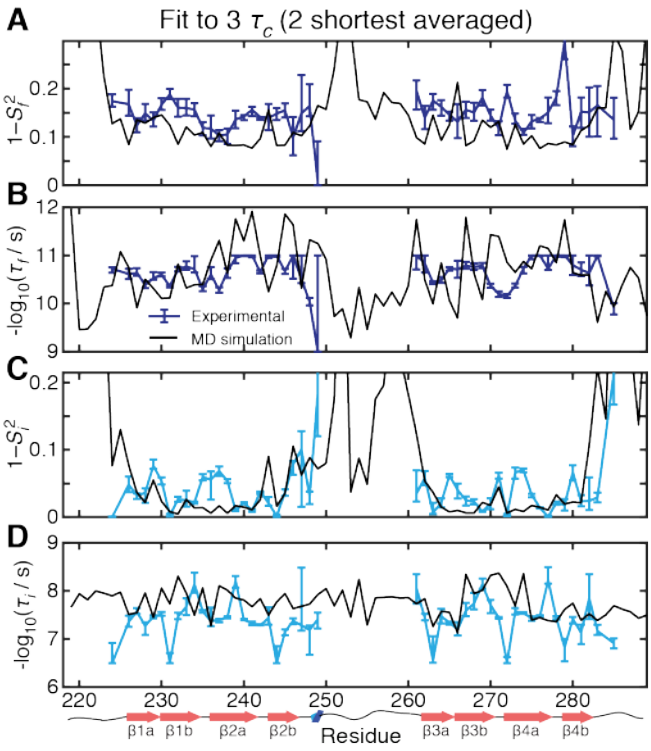

SI Fig. 12. Comparison of MEF results using NMR data fits from ref. [3] and MD data fitted according to Eq. (S18). The motions with the two shortest correlation times obtained via MD are averaged together according to Eq. (S20). **A** compares $1–S_f^2$, **B** compares τ_f, **C** compares $1–S_i^2$, and **D** compares τ_i. In each subplot, colored lines give the NMR derived dynamics parameters, with error bars giving the 68% confidence interval. Black lines give the MD derived parameters.

5. Further analysis

5.1. MD detector analysis with detectors optimized for MD data

The MD trajectory can, in principle, provide us with greater correlation time discrimination than obtained with detector sensitivities optimized for characterization of experimental data (for example, see text Fig. 1). In particular, ρ_0 is sensitive to a wide range of short correlation times, but also is sensitive to longer correlation times (see main text Fig. 1A). To determine whether most of the motion observed with ρ_0 is fast or slow, we re-analyze the AMBER MD trajectory using detector sensitivities that are specifically optimized for characterizing MD. Results are shown in SI Fig. 13, where we see that relatively uniform motional amplitudes are found at the shortest correlation times, whereas large increases in amplitude in $\rho_0^{(\theta,S)}$ found in text Fig. 1B are mostly the result of slower motion (here, corresponding to $\rho_5^{(\theta,S)}$). Note that some caution should be taken when interpreting results for long correlation times: it is difficult to quantify the correlation time of events happening infrequently in the trajectory (this is partially represented by the increasing uncertainty of

detectors with correlation time in SI Fig. 13, and the lack of precision with which we can determine these correlation times is represented by the breadth of the sensitivity of ρ_5). Furthermore, the assumptions leading to eqs. (S11) and (S12), that is, that we sample all configurations, can easily omit some motions occurring at longer correlation times, and therefore $\rho_5^{(\theta,S)}$ will not contain contributions from these motions.

Note that we obtain detectors specifically for MD data in the same manner as is used to obtain the experimental detectors. However, in this case each time point of the MD-derived correlation function is regarded as an experimental data point. Then, the sensitivity of that time point to each possible correlation time (t_n) is given simply by $\exp(-t_n / \tau_c)$, and the standard deviation of each time point is proportional to $\sigma(t_n) \propto \sqrt{n+1}$, since n+1 time points are used to calculate that correlation time at t_n. We then use singular value decomposition to optimize the detectors, as we have previously described in reference [29] (SI section 2).

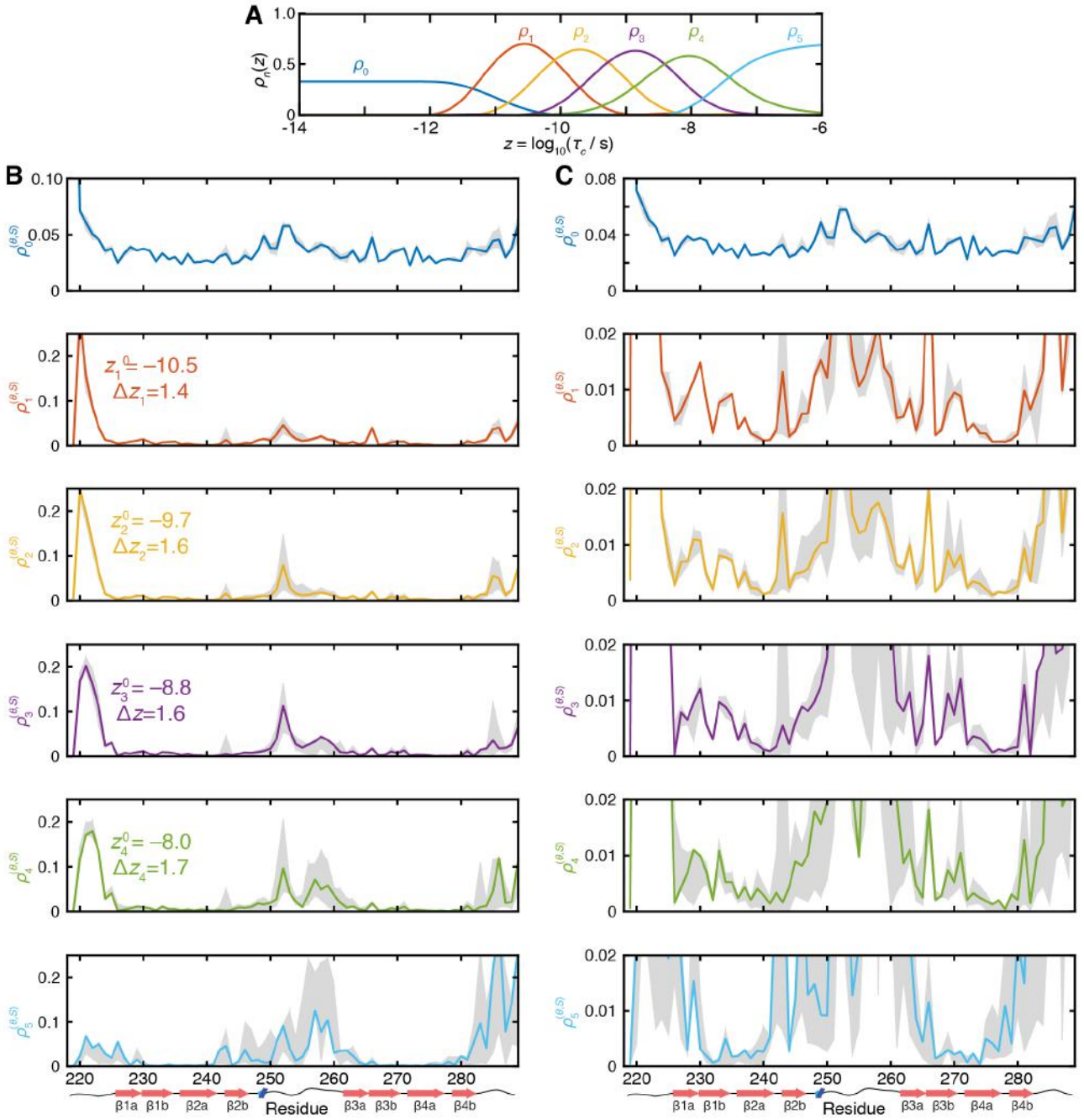

SI Fig. 13. Timescale specific MD-optimized detector sensitivities. **A** shows the detector sensitivity of 6 detectors to be used for MD analysis, where sensitivities have been normalized to have an integral of one. **B** shows the residue-specific detector responses for each detector (colored lines). Grey regions are obtained by analyzing the first and second half of the trajectories separately, which approximates a confidence interval for the detector responses. **C** shows the same data as **B**, but rescales the y-axis to make dynamics in the β-sheet regions more visible.

6. Calculating cross-correlation in MD

6.1. Basic method

We would to know how our measured motions (H–N bond motions in this study) are related to surrounding motion. For this, we need to calculate the cross correlation between H–N motion and other vectors in the molecule (usually defined by bonds), and we want to

obtain cross correlations that have been correlation-time filtered using the same sensitivities, $\rho_n(z)$, that are used to obtain the detector responses. The basic method to obtain such cross-correlation is straightforward, although implementation is more complex. We showed that to obtain detector responses, we find the correlation function of some H–N bond (strictly speaking, the auto-correlation function for the rank-2 tensor that lies parallel with the H–N bond). Then, we take the inverse Laplace transform (invert Eq. (S6), see section 3.2 for details), and finally use the resulting distribution of motion to obtain the detector response (Eq. (S14)). Cross correlation may be obtained the same way, simply replacing the auto-correlation function with the cross-correlation function between the H–N bond and some other vector in the molecule,[20b] which is given as

$$C_{k,j}(t) = \frac{4\pi}{2L+1}\sum_{m=-L}^{L}\left\langle Y_{L,m}(\mathbf{e}_k(\tau))Y^*_{L,m}(\mathbf{e}_j(t+\tau))\right\rangle_\tau \quad \text{(S21)}$$

The $Y_{L,m}(\mathbf{e}_k(\tau))$ are the rank-L spherical harmonics for vectors with direction given by the unit vector $\mathbf{e}_k(\tau)$, which is time-dependent. An average is then taken over all τ (as before, only the τ for which $t+\tau$ is also included in the MD trajectory). Note that we may use either rank-1 or rank-2 cross correlations. The auto-correlation functions obtained with Eq. (S21) are the same as those obtained with Eq. (S5), in the rank-2 case. However, cross-correlations have an angular dependence (depending on the mean angle between the two vectors being correlated), which is somewhat more complex for rank-2 correlations vs. rank-1 correlation (see section 6.2 for details). Therefore, we often calculate rank-1 cross-correlations, as has been done in the main text (Figs. 2 and 3). We may calculate Eq. (S21) using discrete time points as follows, where the t_i are the individual time points:

$$C_{k,j}(t_n) = \frac{4\pi}{2L+1}\sum_{m=-L}^{L}\frac{1}{N-n}\sum_{i=0}^{N-n-1}Y_{L,m}(\mathbf{e}_k(t_i))Y^*_{L,m}(\mathbf{e}_j(t_{i+n})) \quad \text{(S22)}$$

Then, we assume that the cross-correlation function can also be constructed from a sum of decaying exponential terms, such that

$$C_{k,j}(t) = C_{k,j}(t\to\infty) + \int_{-\infty}^{\infty}\theta_{k,j}(z)\exp(-t/(10^z\cdot 1\,\mathrm{s}))\,dz \quad \text{(S23)}$$

The discretized form is given as

$$C_{k,j}(t_n) = C_{k,j}(t\to\infty) + \sum_{m=1}^{M}[\vec{\theta}_{k,j}]_m\exp(-t_n/(10^{z_m}\cdot 1\,\mathrm{s})) \quad \text{(S24)}$$

Eq. (S23) differs slightly from Eq. (S6), in that we do not define S^2 for the cross-correlated motion. The reason is that auto-correlation functions must have an initial value of 1, so the

plateau value (S^2) and the decaying components must sum to 1. We achieved this by requiring that $\theta(z)$ integrated to one, and then multiplied the whole integral by $(1-S^2)$. However, the initial value of the cross-correlation function may fall anywhere between 1 and -1 (the initial value gives the average correlation of bonds *k* and *j* at the same time, so this only must be one in the case that *k* = *j*). Then, we still define a plateau value, denoted here as $C_{k,j}(t\to\infty)$, but the distribution function, $\theta_{k,j}(z)$, need not integrate to one and is not multiplied by a pre-factor.

$\theta_{k,j}(z)$ is the inverse Laplace transform of $C_{k,j}(t)$, which may be used to obtain a cross-correlated detector response, that is, the cross-correlation between two bonds that has been filtered by the sensitivity of a given detector. This is defined as follows, following the form of Eq. (S14)

$$\begin{aligned}\rho_n^{k,j} &= \int_{-\infty}^{\infty}\theta_{k,j}(z)\rho_n(z)dz \\ &\approx \sum_{m=1}^{M}[\vec{\theta}_{k,j}]_m\rho_n(z_m)\end{aligned} \quad . \tag{S25}$$

$\rho_n^{k,j}$ is the detector response of the cross-correlated motion (*k* and *j* typically indicate some pair of bonds). This cross-correlated detector response is specific to the range of correlation times defined for a given detector's sensitivity, $\rho_n(z)$. For easier interpretation, we calculate a correlation coefficient (based on Pearson's r), defined as

$$\rho_{n,\text{norm}}^{k,j} = \frac{\rho_n^{k,j}}{\sqrt{\rho_n^{k,k}\rho_n^{j,j}}}\ , \tag{S26}$$

where the $\rho_n^{k,k}$ are the detector responses corresponding to the auto-correlation of some bond (or vector) *k*, evaluated using detector sensitivity, $\rho_n(z)$ (note when correlating rank-2 tensors, the $\rho_n^{k,k}$ are the usual detector responses, such that $\rho_n^{k,k}=\rho_n^{(\theta,S)}$ for the k^{th} vector). $\rho_n^{k,j}$ is the detector response obtained from the cross-correlation function. Then, $\rho_{n,norm}^{k,j}$ ranges from +1 for fully correlated motion, -1 for fully anti-correlated motion, and 0 for no correlation. Note that in Eq. (S26), if the $\rho_n^{k,k}$ become small, then calculation of $\rho_{n,\text{norm}}^{k,j}$ can become very sensitive to fitting variations in the inverse Laplace transform, causing results deviating above 1 and below -1. This is resolved using an eigenmode approach to obtaining the correlation functions and cross-correlated detector responses, as discussed in SI section 6.3.

6.2. Angular dependence of cross-correlation

The sign of the cross correlation between two vectors depends on the angle between these vectors and the rank of the tensor correlation used. This dependence arises from the functional form of the 1st or 2nd order Legendre polynomial of the cosine of the angle between the two vectors:

$$P_1(\cos(\theta_{k,j})) = \cos(\theta_{k,j})$$
$$P_2(\cos(\theta_{k,j})) = \frac{1}{2}\left(3\cos^2(\theta_{k,j}) - 1\right), \quad \text{(S27)}$$

For example, if the angle between the two bonds fluctuates around 0°, then both $P_1(\cos(\theta_{k,j}))$ and $P_2(\cos(\theta_{k,j}))$ will be positive (and scaled down from 1, depending on the amplitude of the fluctuation away from 0°). If, on the other hand, the angle fluctuations around 180°, $P_1(\cos(\theta_{k,j}))$ will become negative, but $P_2(\cos(\theta_{k,j}))$ will remain positive. Further angular dependencies are summarized in SI Fig. 14.

In this study, the angular dependence of the correlation coefficients has little consequence on our analysis, because in the HET-s(218-289) fibrils, most H–N bonds are either parallel or anti-parallel to each other (leading to positive and negative correlation, but little scaling of the absolute value of the correlation). In other proteins where bonds may take on a large number of relative orientations, this will make correlation of motion more difficult to interpret. A simple solution is to calculate both rank-1 and rank-2 correlations to verify that important correlations are not missed, although this is only a qualitative improvement and does not allow quantitative comparison of correlation behavior. A more rigorous approach would be to calculate the average direction of each bond vector for the whole trajectory. Then, one determines a transformation that rotates each average vector to the *z*-axis. The same transformation can then be applied to that bond for each time point in the trajectory. The result is a new set of vectors for every bond, that now all have the same average direction. These can be correlated instead of the original bonds, and now have no angular dependence. However, an investigation is still necessary to determine how such a transformation can affect the sign of the cross-correlation, especially for rank-1 correlation, where rank-2 correlations should be more straightforward, yielding only positive correlations for parallel vectors (a drawback is that the ability to distinguish between correlation and anti-correlation is lost for rank-2).

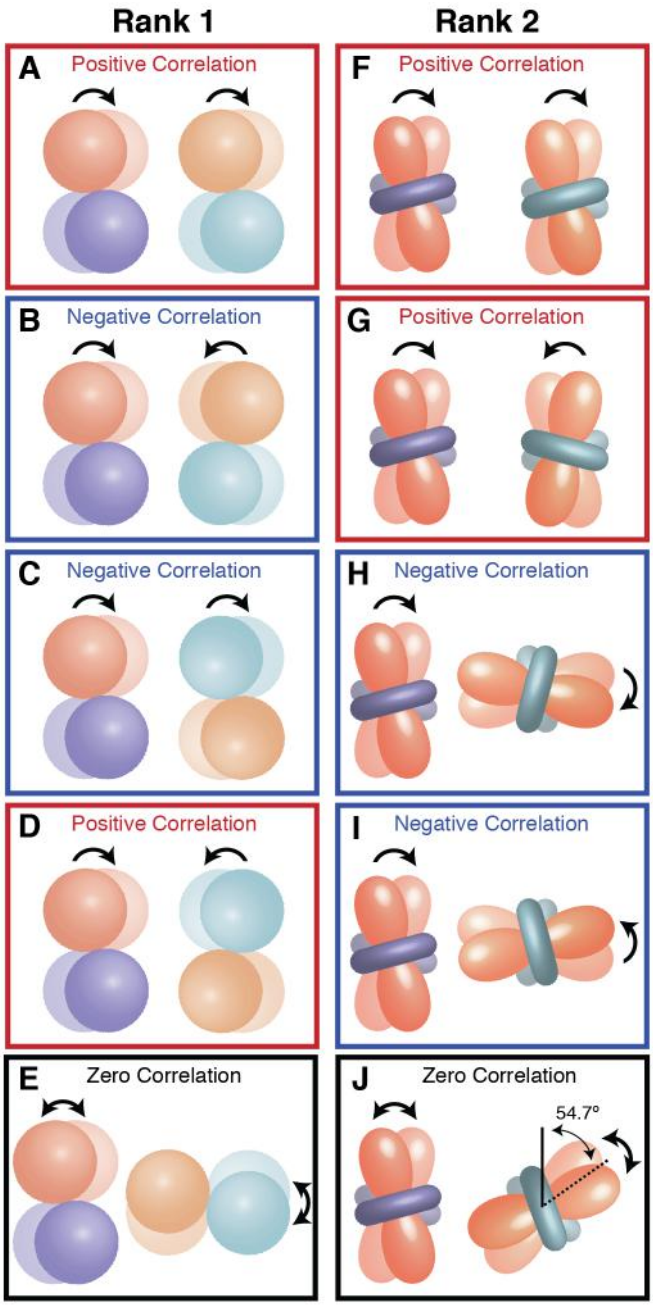

SI Fig. 14. Types of correlation for rank-1 and rank-2 tensors. **A**-**E** show rank-1 tensors, and **F**-**J** show rank-2 tensors. The relative motion and orientation of the two tensors shown determine the behavior of the sign of the correlation. Two rank-1 tensors moving the same direction with the same orientation are positively correlated (**A**). However, inverting the direction of motion (**B**) or the orientation (**C**) of one of the tensors yields negative correlation (inverting both yields positive correlation again, (**D**). For rank-2 tensors, the sign of the correlation is not sensitive to the direction of the motion (**G**, **I**), but a 90º rotation of one of the tensors (**H**,**I**) will yield a negative correlation (although with only half the magnitude of the positive correlation). Zero correlation may be obtained for rank-1 tensors if they are oriented 90º from each other (**E**), whereas zero correlation is obtained for the rank-2 tensors if they are oriented at the magic angle (**J**, θ=54.7º). Note: if the motions of the two tensors are totally uncoupled, then we should always obtain zero correlation. However, if the angle between the two tensors is 90° (rank-1) or 54.7° (rank-2), we will obtain zero correlation even if the motion is coupled.

6.3. iRED method

In section 6.1, we derived the definition of a cross-correlated detector response, $\rho_n^{k,j}$ (Eq. (S25)), and the corresponding correlation coefficient, $\rho_{n,norm}^{k,j}$ (Eq. (S26)). Evaluation of Eq. (S25), however, first requires inversion of Eq. (S23). Although we could adapt the methodology used in section 3.2, we require a more stable method here. The problem arises if the auto-correlated detector responses ($\rho_n^{k,k}$ in Eq. (S26)) are too small, variation in the results of the inverse Laplace transform can cause the correlation coefficients to become unphysical. This is because it becomes possible for small variations in the inverse Laplace transform to lead to $\left|\rho_n^{k,j}\right|$ becoming larger than $\sqrt{\rho_n^{k,k}\rho_n^{j,j}}$, so that the correlation coefficients have absolute values larger than 1. Note that such smaller errors are only significant when we need to take a ratio of detector responses, which is not required when calculating the detector response, $\rho_n^{(\theta,S)}$ (Eq. (S14)). A secondary problem arises, if we want to correlate, for example, motion of all pairs of backbone H–N bonds in our simulations (see SI Fig. 16-SI Fig. 19), we must calculate and fit ~40,000 correlation functions (a feasible, but cumbersome calculation due to the high computation cost of correlation functions).

We can circumvent both of these problems, using an approach based on the work of Prompers and Brüschweiler.[30] The isotropic Reorientational Eigenmode Dynamics (iRED) method allows one to construct individual auto- and cross-correlation functions from a basis set of correlation functions. If we take M vectors in the molecule (usually bonds), then one can calculate M^2 correlation functions (M auto-correlation functions, and $M(M–1)$ cross-correlation functions). The iRED method allows us to construct all of these correlation functions from M basis correlation functions, $\Delta C_m(t)$. Clearly, this lowers the computational cost (by a factor of ~M). However, it will also become possible to perform inverse Laplace transform and calculate detector responses of the basis correlation functions. Then, the auto- and cross-correlated detector responses required for calculating correlation coefficients (Eq. (S26)) are constructed from these basis detector responses. By constructing the required detector responses from the detector responses of the basis correlation functions, we prevent $\left|\rho_n^{k,j}\right|$ from becoming larger than $\sqrt{\rho_n^{k,k}\rho_n^{j,j}}$. Although imperfect inverse Laplace transforms may still cause small variations in the detector responses of the basis correlation functions, we obtain a set of responses that are nonetheless physically consistent.

The iRED methodology allows us to construct individual correlation functions from the basis correlation functions (minus their plateau values), $\Delta C_m(t)$, as follows:

$$C_{k,j}(t) - C_{k,j}(t \to \infty) = \sum_{m=1}^{M-(2*L+1)} \lambda_m (|m\rangle)_k (\langle m|)_j \Delta C_m(t) \qquad \text{(S28)}$$

The λ_m are eigenvalues (sorted from smallest to largest) and $|m\rangle$ are eigenvectors of the iRED matrix (**M**), and the $\Delta C_m(t)$ are normalized basis correlation functions of the corresponding eigenvalues (normalization implies that $\Delta C_m(0) = 1$ and $\Delta C_m(t)$ has a final value of 0, see below for calculation of $\Delta C_m(t)$). These terms are derived by Prompers and Brüschweiler;[30b] we will describe how to calculate **M** and derive the other terms later for completeness, but we will first show how we may use them to construct the required cross-correlated detector responses and correlation coefficients. Note that the summation omits the largest 2*L*+1 modes (*L* is the tensor rank). These modes contain overall motion of the structure - motions that result from rotation of the structure, but do not yield any internal structural rearrangement. Since we use solid-state samples, we assume there is no overall motion, and therefore omit these modes. Note that to use the iRED approach, we must analyze a sufficient number of vectors (e.g. bonds) in the molecule simultaneously. This is because removal of the 2*L*+1 modes can remove some internal motion, and so the more modes utilized, the smaller the fraction of the internal motion removed (e.g. suppose we have *L*=2, and only include five bonds, then all five of our modes would be removed, leaving no internal motion).[31]

Now, we derive the cross-correlated detector responses using the iRED method. Let us first assume that we can construct $\Delta C_m(t)$ from a sum of decaying exponential terms:

$$\Delta C_m(t) = \int_{-\infty}^{\infty} \theta_m(z) \exp(-t / (10^z \cdot 1\,\mathrm{s}))\, dz\,. \qquad \text{(S29)}$$

We use $\Delta C_m(t)$ defined such that $\Delta C_m(0) = 1$ and $\Delta C_m(t \to \infty) = 0$. Then, we can obtain the inverse Laplace transform according to SI section 3.2, and treat the correlation function as if S^2=0.

It follows that we can construct any correlation function from the distribution functions of the basis correlation functions, $\theta_m(z)$:

$$C_{k,j}(t) - C_{k,j}(t \to \infty) = \sum_{m=1}^{M-(2*L+1)} \lambda_m (|m\rangle)_k (\langle m|)_j \int_{-\infty}^{\infty} \theta_m(z) \exp(-t / (10^z \cdot 1\,\mathrm{s}))\, dz \qquad \text{(S30)}$$

.

A simple switch of the order of the sum and integral yields (second line restates Eq. (S23)):

$$C_{k,j}(t) - C_{k,j}(t \to \infty) = \int_{-\infty}^{\infty} \sum_{m=1}^{M-(2*L+1)} \lambda_m (|m\rangle)_k (\langle m|)_j \theta_m(z) \exp(-t/(10^z \cdot 1\,\mathrm{s}))dz$$
$$= \int_{-\infty}^{\infty} \theta_{k,j}(z) \exp(-t/(10^z \cdot 1\,\mathrm{s}))dz \quad , \tag{S31}$$

so that it is possible to obtain $\theta_{k,j}(z)$:

$$\theta_{k,j}(z) = \sum_{m=1}^{M-(2*L+1)} \lambda_m (|m\rangle)_k (\langle m|)_j \theta_m(z) \tag{S32}$$

Furthermore, we may calculate the detector response for the cross-correlation function, $\rho_n^{k,j}$, where we again switch the order of the sum and integral in the second line.

$$\rho_n^{k,j} = \int_{-\infty}^{\infty} \theta_{k,j}(z) \rho_n(z) dz = \int_{-\infty}^{\infty} \sum_{m=1}^{M-(2*L+1)} \lambda_m (|m\rangle)_k (\langle m|)_j \theta_m(z) \rho_n(z) dz$$
$$= \sum_{m=1}^{M-(2*L+1)} \lambda_m (|m\rangle)_k (\langle m|)_j \int_{-\infty}^{\infty} \theta_m(z) \rho_n(z) dz \tag{S33}$$

Then, we define the basis detector response, ρ_n^m, to obtain a simple formula for the cross-correlated detector responses, $\rho_n^{k,j}$:

$$\rho_n^m = \int_{-\infty}^{\infty} \theta_m(z) \rho_n(z) dz$$
$$\rho_n^{k,j} = \sum_{m=1}^{M-(2*L+1)} \lambda_m (|m\rangle)_k (\langle m|)_j \rho_n^m \,. \tag{S34}$$

We may construct all auto- and cross-correlated detector responses, $\rho_n^{k,j}$, from the basis detector responses, ρ_n^m, resulting from the M basis correlation functions, $|m\rangle$. Therefore, we only perform the inverse Laplace transform on the basis correlation functions, $C_m(t)$. After obtaining the $\rho_n^{k,j}$, we may calculate the correlation coefficients (Eq. (S26)).

Eq. (S28) is derived by Prompers and Brüschweiler and the terms in it are defined,[30] but we summarize the results that are necessary for its application to detectors here. The λ_m and $|m\rangle$ are eigenvalues and eigenvectors of a matrix, **M**, for which each element is calculated for rank-L cross-correlation:

$$M_{k,j} = \left\langle P_L(\mathbf{e}_k(\tau) \cdot \mathbf{e}_j(\tau)) \right\rangle_\tau \tag{S35}$$

.

Here, the $\mathbf{e}_k(\tau)$ are unit vectors, indicating the direction of the k^{th} vector (usually a bond) at time τ in the trajectory. Then, the dot product yields the cosine of the angle between the two vectors, and P_L is the rank-L Legendre polynomial ($P_1(x) = x$, $P_2(x) = (3x^2 - 1)/2$, etc.).

An average is taken over all times, τ, of the trajectory, so that the $M_{k,j}$ can be calculated numerically as

$$M_{k,j} = \frac{1}{N}\sum_{i=0}^{N-1} P_L(\mathbf{e}_k(\tau_i)\cdot\mathbf{e}_j(\tau_i)) \tag{S36}$$

.

Once **M** is calculated, we calculate its eigenvalues and eigenvectors (the eigenvectors, $|m\rangle$, having a 2-norm of 1), so that $\mathbf{M}|m\rangle = \lambda_m|m\rangle$.

Once we have **M** and its eigenvalues and eigenvectors, we then need to calculate the mode correlation functions, $C_m(t)$. First, we calculate the amplitude of each of the 2*L*+1 spherical components of each mode. For the m^{th} mode, we calculate all the spherical components of each of the *M* vectors, $\mathbf{e}_k(t)$.

Rank 1:

$$Y_{10}(\theta_k(t),\phi_k(t)) = \frac{1}{\sqrt{2}}c\cos\theta_k(t)$$
$$Y_{1\pm1}(\theta_k(t),\phi_k(t)) = \mp\frac{1}{2}c\exp(\pm i\phi_k(t))\sin\theta(t)$$
$$c = \sqrt{3/(2\pi)}$$

Rank 2:

$$Y_{20}(\theta_k(t),\phi_k(t)) = c\sqrt{2/3}(3\cos^2\theta_k(t)-1)$$
$$Y_{2\pm1}(\theta_k(t),\phi_k(t)) = 2c\cos\theta_k(t)\sin\theta_k(t)\exp(\pm i\phi_k(t))$$
$$Y_{2\pm2}(\theta_k(t),\phi_k(t)) = c\sin^2\theta_k(t)\exp(\pm 2i\phi_k(t))$$
$$c = \sqrt{15/(32\pi)} \tag{S37}$$

$$\cos\theta_k(t) = [\mathbf{e}_k(t)]_z,\quad \sin\theta_k(t) = \sqrt{([\mathbf{e}_k(t)]_x)^2 + ([\mathbf{e}_k(t)]_y)^2},$$
$$\exp(\pm i\phi_k(t)) = [\mathbf{e}_k(t)]_x \pm i[\mathbf{e}_k(t)]_y,\quad \exp(\pm 2i\phi_k(t)) = \exp(2\log([\mathbf{e}_k(t)]_x \pm i[\mathbf{e}_k(t)]_y))$$

Then, we obtain the amplitudes of the l^{th} spherical component of the m^{th} eigenmode by projecting the m^{th} mode onto the l^{th} spherical components for all *M* vectors, $\mathbf{e}_k(t)$ (at some time *t*).

$$a_{m,l}(t) = \langle m|Y_{L,l}(t)\rangle \tag{S38}$$

.

Numerically, this is implemented as

$$a_{m,l}(t) = \sum_{k=1}^{M}(\langle m|)_k Y_{L,l}(\theta_k(t),\phi_k(t)) \tag{S39}$$

.

($\langle m|)_k$ is simply the complex conjugate of the k^{th} element of $|m\rangle$. From the $a_{m,l}(t)$, we can calculate the correlation functions of each mode, *m*, for each spherical component, *l*.

$$C_{m,l}(t) = \left\langle a^*_{m,l}(t+\tau) a_{m,l}(\tau) \right\rangle_\tau$$
$$C_{m,l}(t_n) = \frac{1}{N-n} \sum_{i=0}^{N-n-1} a^*_{m,l}(t_{i+n}) \cdot a_{m,l}(t_i) \quad \text{(S40)}$$

We obtain $C_m(t)$ by simply summing together all correlation functions, $C_{m,l}(t)$.

$$C_m(t) = \sum_{l=-L}^{L} C_{m,l}(t) \quad \text{(S41)}$$

$C_m(t)$ may not decay fully to zero, but we may obtain its equilibrium value as

$$C_m(t \to \infty) \cong \sum_{l=-L}^{L} |\langle a_{m,l}(\tau) \rangle_\tau|^2 = \sum_{l=-L}^{L} \left| \frac{1}{N} \sum_{i=0}^{N-1} a_{m,l}(t_i) \right|^2 \quad \text{(S42)}$$

Note that this equilibrium value is much more stable than simply taking the final value of the correlation function, which results from averaging only a single pair of time points. Finally, we define $\Delta C_m(t)$:

$$\Delta C_m(t) = \frac{C_m(t) - C_m(t \to \infty)}{C_m(0) - C_m(t \to \infty)}, \quad \text{(S43)}$$

which has an initial value of $\Delta C_m(0) = 1$ and a final value of $\Delta C_m(t \to \infty) = 0$

7. Cross-correlation results

7.1. AMBER H–N and peptide plane correlation (rank-2)

In main text Fig. 2, we calculate the correlation of H–N motion with its peptide plane, using rank-1 tensors. For comparison, we calculate the same correlation using rank-2 tensors. Results are very similar, with differences arising from the angular dependence of the tensor correlation (see SI section 6.2). The degree of similarity is due to the fact that the H–N bond vector and the bisector of the C'–Cα and C'–N bonds are nearly co-linear, so that both $P_1(\cos(\theta_{k,j}))$ and $P_2(\cos(\theta_{k,j}))$ fluctuate around 1. Therefore, if the bonds being correlated are not co-linear, one may expect more significant differences and sign changes when comparing rank-1 and rank-2 tensor correlations.

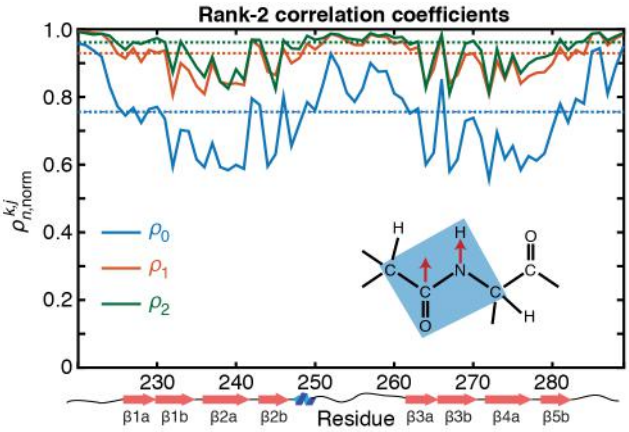

SI Fig. 15. Rank-2 correlation of H–N bond motion with its peptide plane. The inset shows the two vectors being correlated, which are the H–N bond and a vector bisecting the C'–N and C'–Cα bonds. Correlation coefficients are shown with timescale filtering using the sensitivities of ρ_0, ρ_1, and ρ_2, which are plotted in SI Fig. 6A. Dotted lines indicate the median values of the cross-correlation.

7.2. AMBER cross-correlation analysis

Main text Fig. 3 selects the H–N bonds of a few residues and shows how these motions are related to motions of the surround H–N bonds. However, by using the iRED approach, we easily obtain *all* cross-correlations. SI Fig. 16 color-codes the rank-1 correlation matrix for all correlations between the center HET-s molecule to all three molecules (hence, we display a 70x210 matrix. Note we can obtain a full 210x210 matrix, but we expect correlations of the outer two molecules to be less useful, since they are not sandwiched by two HET-s molecules). Black squares indicate the main diagonal (autocorrelation, for which $\rho^{k,k}_{n,norm} \equiv 1$), near which we see the highest correlation, since squares near the main diagonal indicate residues neighboring in the chain. Light grey diagonal lines in SI Fig. 16 indicate where two residues sit directly above each other in the fibril, so that we expect higher correlation along these diagonals. This is observed for ρ_1 and ρ_2. Checkerboard patterns arise for ρ_2 on the main diagonal when motion is correlated for residues separated by several residues. Similar checkerboard patterns also arise on the off diagonals (light grey lines) when motion is correlated over several fibril layers. This is particularly apparent for ρ_2, where correlation was also seen over several residues and fibril layers in main text Fig. 3.

SI Fig. 17 shows cross-correlation calculated for rank-2. Similar results are obtained, although most correlations are positive due to different angular dependence, as is discussed in SI section 6.2. We find interpretation of rank-1 correlations simpler, but provide this result to verify that the expected rank-2 result is obtained.

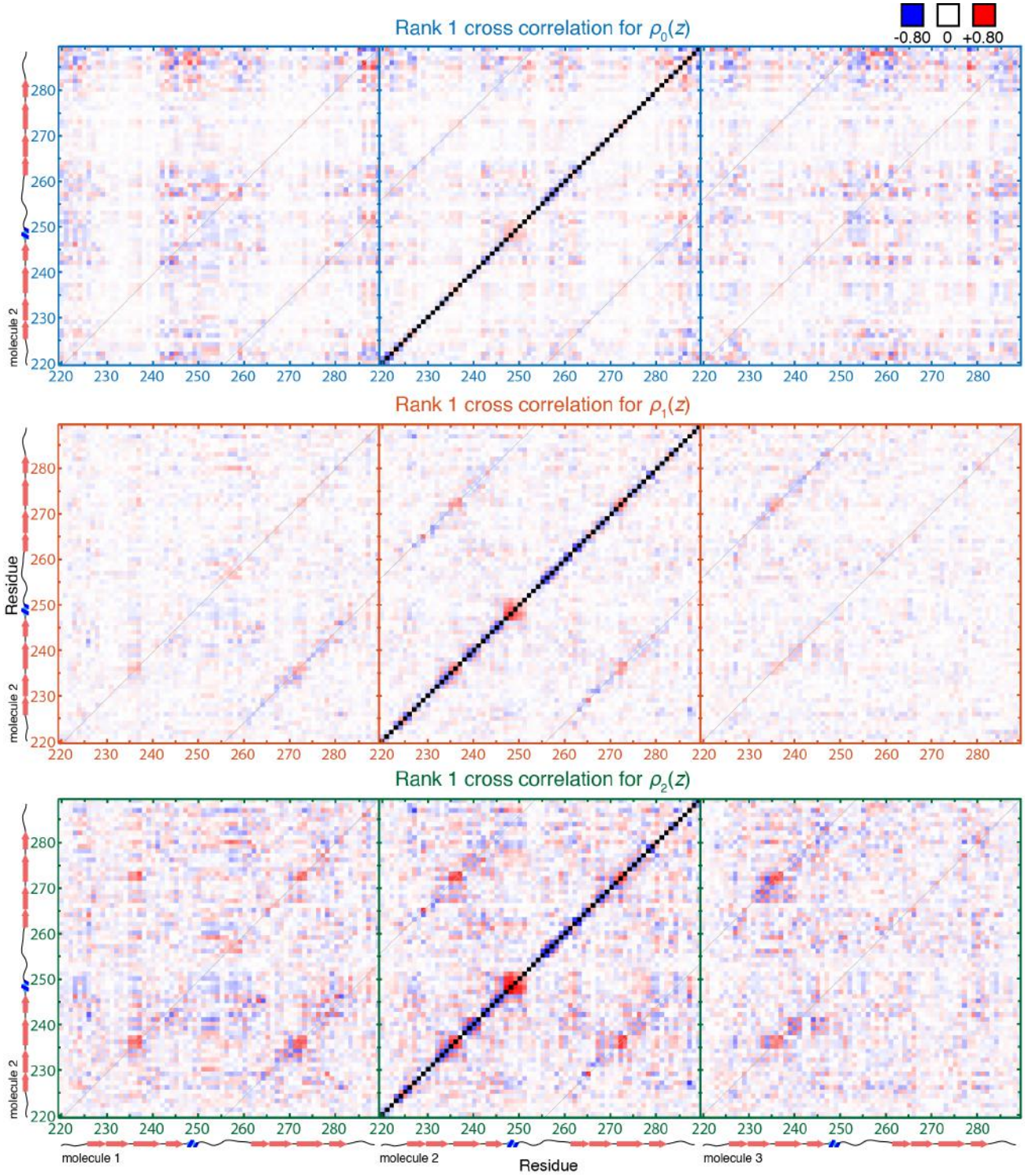

SI Fig. 16. Rank-1 correlated H–N bond motion between molecule 2 of the MD trajectory (y-axis) and all molecules (AMBER force field). All elements are normalized by the square-root of the two corresponding diagonal elements (so the black, diagonal elements are all 1). All non-diagonal elements are coded with a blue-white-red color scale, corresponding to -0.80, 0, +0.80. Light grey lines through the plots indicate residues positioned exactly one layer above in the β-sheet (for example, residue 235 sits next to residue 271 of the same molecule, and 271 of the previous molecule. Two layers away corresponds to 235 from the two neighboring molecules).

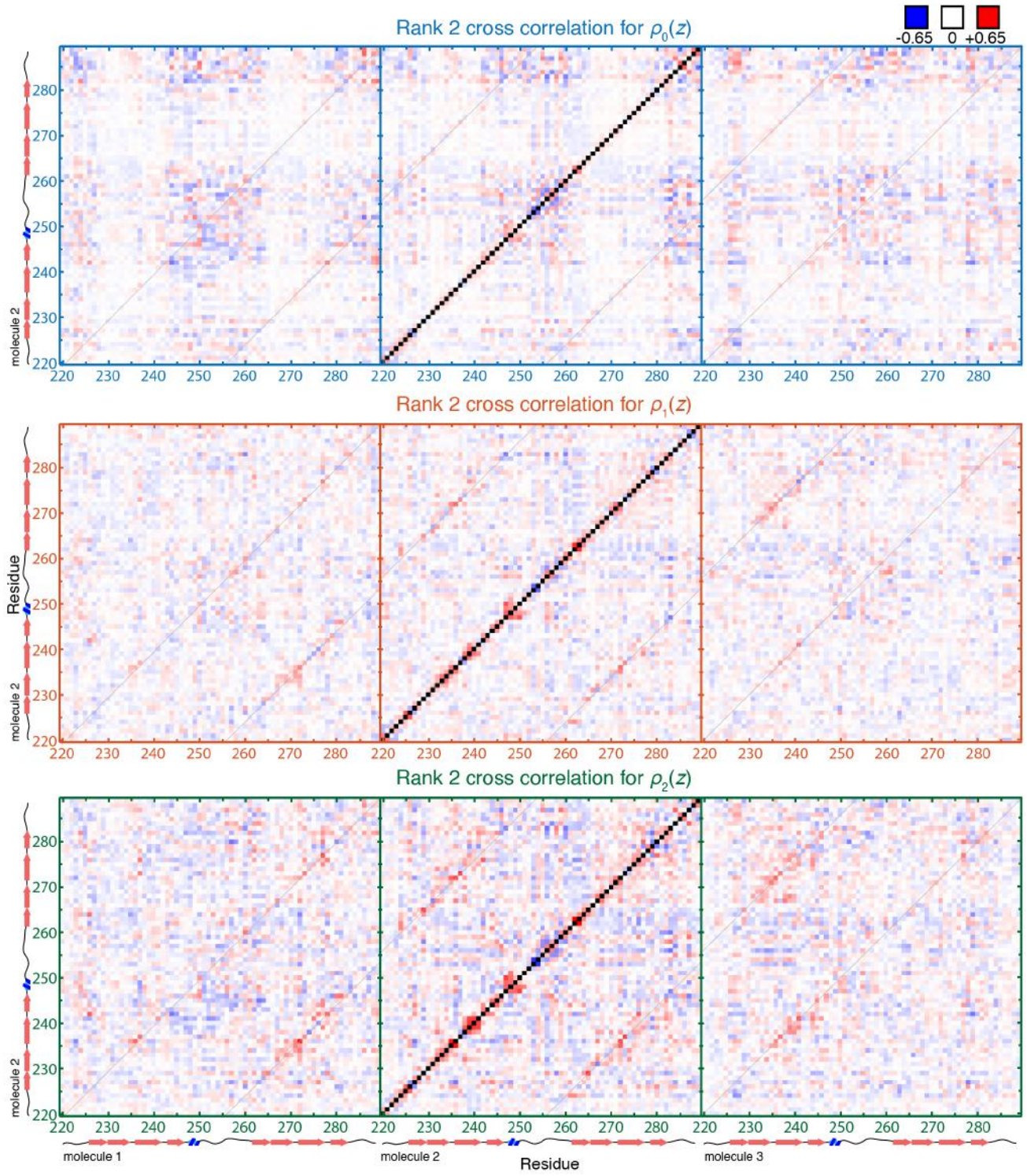

SI Fig. 17. Rank 2 correlated H–N bond motion between molecule 2 of the MD trajectory (y-axis) and all molecules (AMBER force field). All elements are normalized by the square-root of the two corresponding diagonal elements (so the black, diagonal elements are all 1). All non-diagonal elements are coded with a blue-white-red color scale, corresponding to -0.65, 0, +0.65. Light grey lines through the plots indicate residues positioned exactly one layer above in the β-sheet.

7.3. AMBER noise analysis

We perform noise analysis by processing the first and second 250 ns of the full 500 ns trajectory separately, and taking the sum and difference of the resulting $\rho_n^{k,j}$. Both the sum and difference are normalized to obtain correlation coefficients using the $\rho_n^{k,k}$ from the results of the sum calculation. Results are plotted in SI Fig. 18 (sum) and SI Fig. 19 (difference). The amount of correlation in the difference results is a good estimate of the overall noise level, i.e. apparent correlations in the motion that in fact are not real, but are rather the result of a finite trajectory. For example, we see that detectors corresponding to longer correlation times exhibit more noise- this is because fewer occurrences of these motions are present in the trajectory, and so our statistics are less reliable. Note that it is not usually a good idea to interpret single correlations. This is because we show 14,700 correlations in SI Fig. 18 and SI Fig. 19, so we will have numerous false correlations even if the confidence in the individual correlations is highly accurate. Instead, the overall trends should be interpreted. Trends appearing in both the sum and difference calculations may still be real correlations, although the amplitudes of those correlations have a high uncertainty.

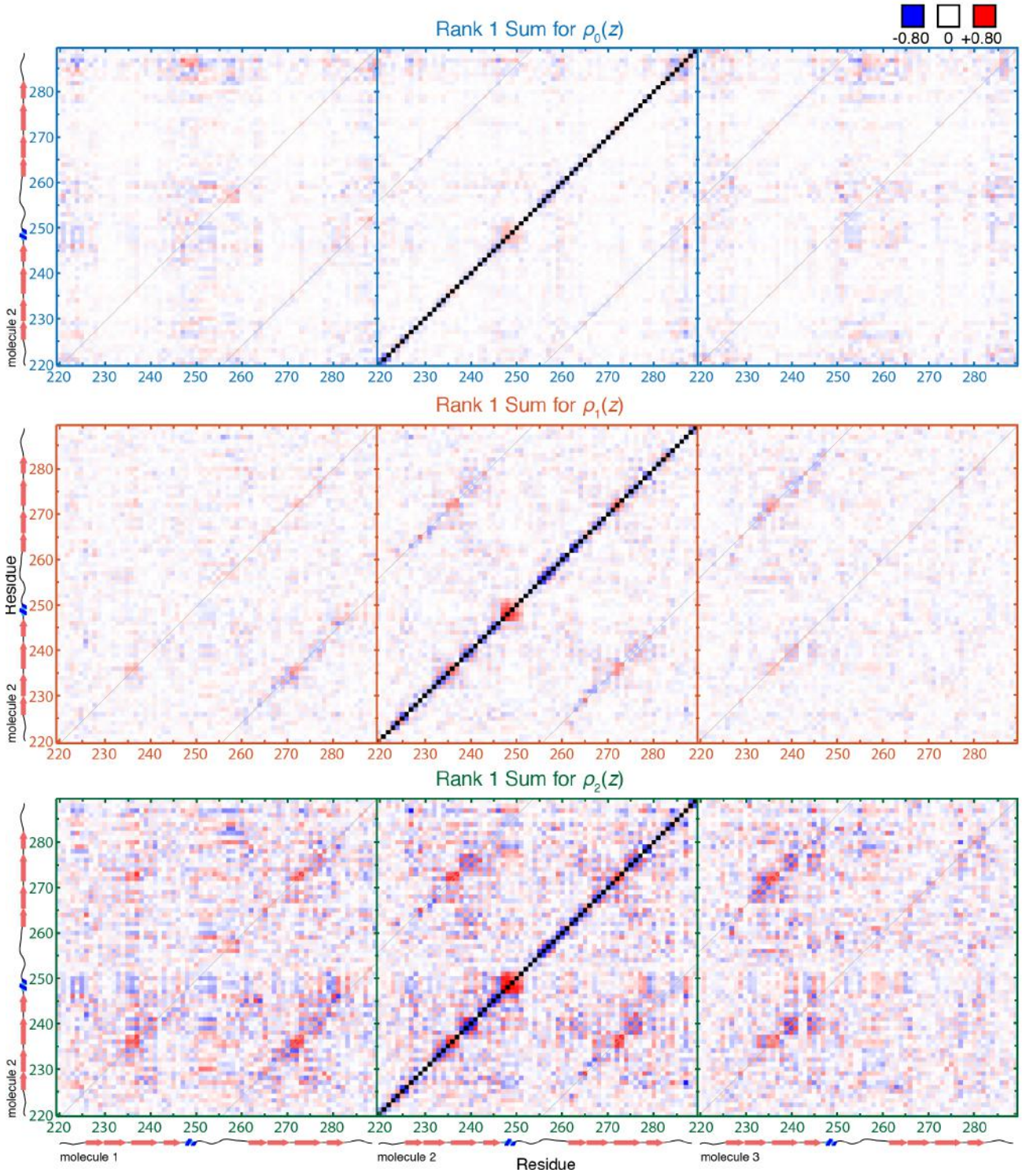

SI Fig. 18. Noise analysis: sum of correlations. Rank 1 correlations were calculated for the first and second halves of the MD trajectory (AMBER force field). The correlations ($\rho_n^{k,j}$) are either added together or subtracted (added in this plot), and normalized by the square-root of the product of the two corresponding diagonal elements ($\sqrt{\rho_n^{k,k} \cdot \rho_n^{j,j}}$). Patterns of cross-correlation appearing in this plot, but not in the difference plot (SI Fig. 19) are likely to be real correlations.

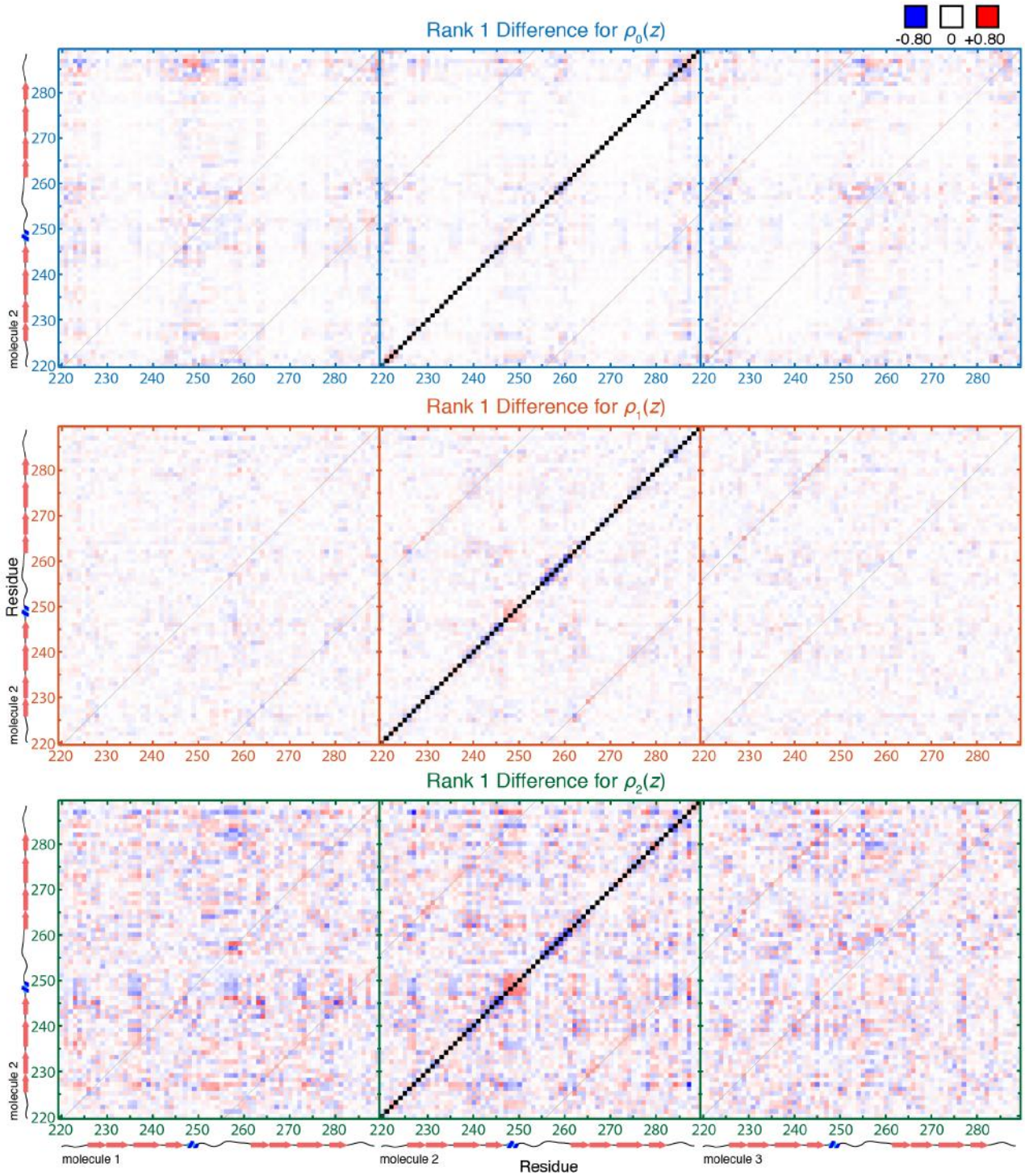

SI Fig. 19. Noise analysis: difference of correlations. Rank 1 correlations were calculated for the first and second halves of the MD trajectory (AMBER force field). The correlations ($\rho_n^{k,j}$) are either added together or subtracted (subtracted in this plot), and normalized by the square-root of the product of the two corresponding diagonal elements of the *sum* of correlations ($\sqrt{\rho_n^{k,k} \cdot \rho_n^{j,j}}$).

7.4. Additional 3D plots for AMBER trajectory

Main text Fig. 3 shows correlations of several H–N bonds to the H–N bonds of all other residues. We show several more residues in SI Fig. 20 to give a more complete picture of the correlated motion.

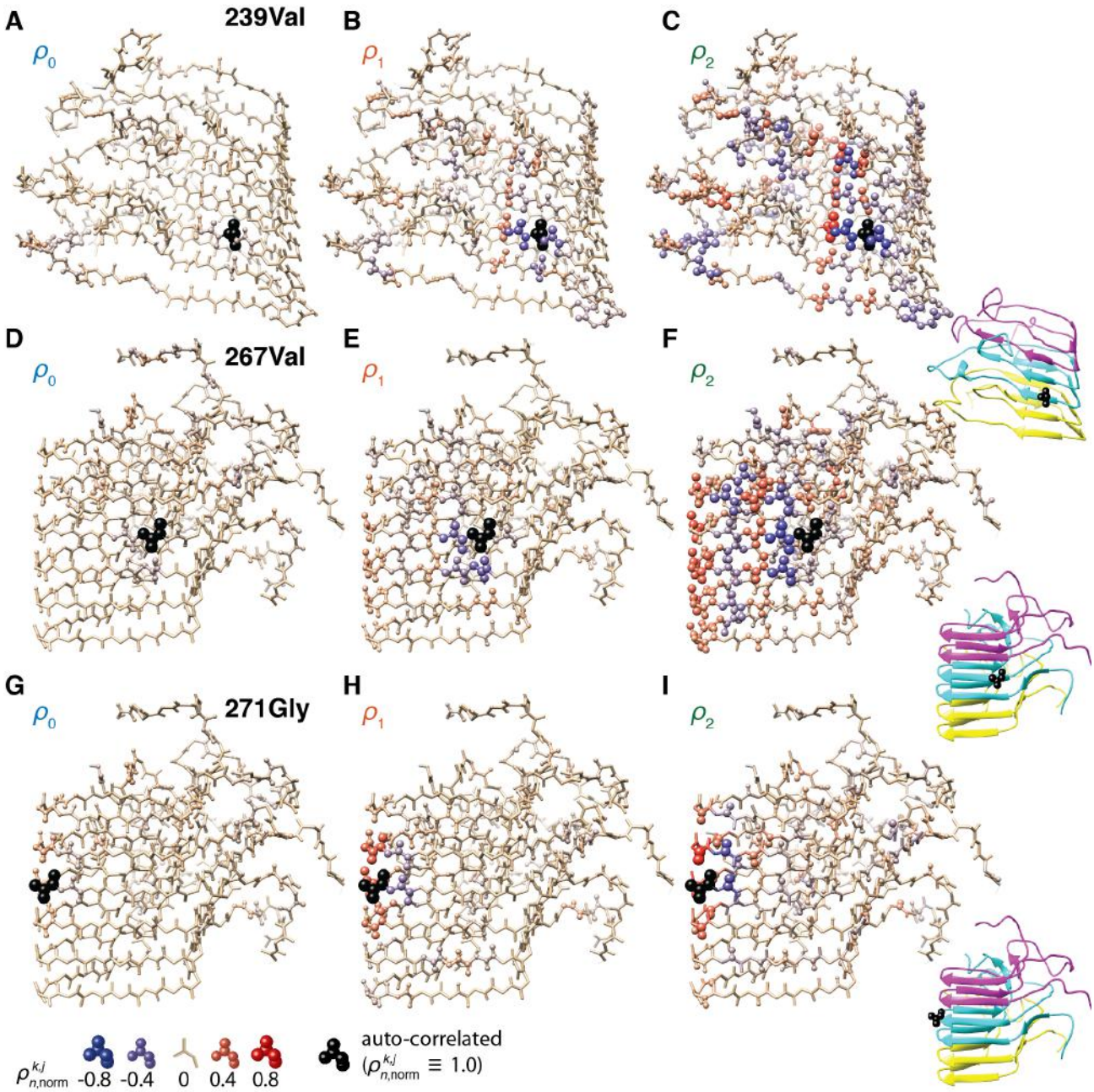

SI Fig. 20. Detector-specific correlation coefficients for several residues (rank-1), calculated from the AMBER trajectory. Each subplot gives the correlation coefficients between an H–N bond of the middle HET-s(218-289) molecule (shown in black) to all other H–N bonds, for ρ_0, ρ_1, and ρ_2. The volume of each atom is proportional to $|\rho^{k,j}_{n,\mathrm{norm}}|$, whereas color-coding also indicates the sign of $\rho^{k,j}_{n,\mathrm{norm}}$. All atoms in the same peptide plane as the H–N bond are sized and colored according to $\rho^{k,j}_{n,\mathrm{norm}}$ for better visibility. **A**-**C** are correlations to the H–N bond of residue 239Val, **D**-**F** for residue 267Val, and **G**-**I** for residue 271Gly. Yellow/cyan/magenta fibril plots (lower right) serve as a reference to see the overall fibril structure and orientation.

7.5. Total correlation for AMBER trajectory

Note that simply calculating the overall correlation between motion of different residues may not always reveal all timescale-specific correlation. For example, here we calculate the total correlation (effectively, using a detector with uniform sensitivity, $\rho_n(z) = 1$ for all z)

using the AMBER trajectory, where most of the correlations seen in text Fig. 3 and SI Fig. 20 vanish. Note, however, that for some systems, the total correlation may still be useful, as was shown by Salvi et al. for intrinsically disordered proteins.[32]

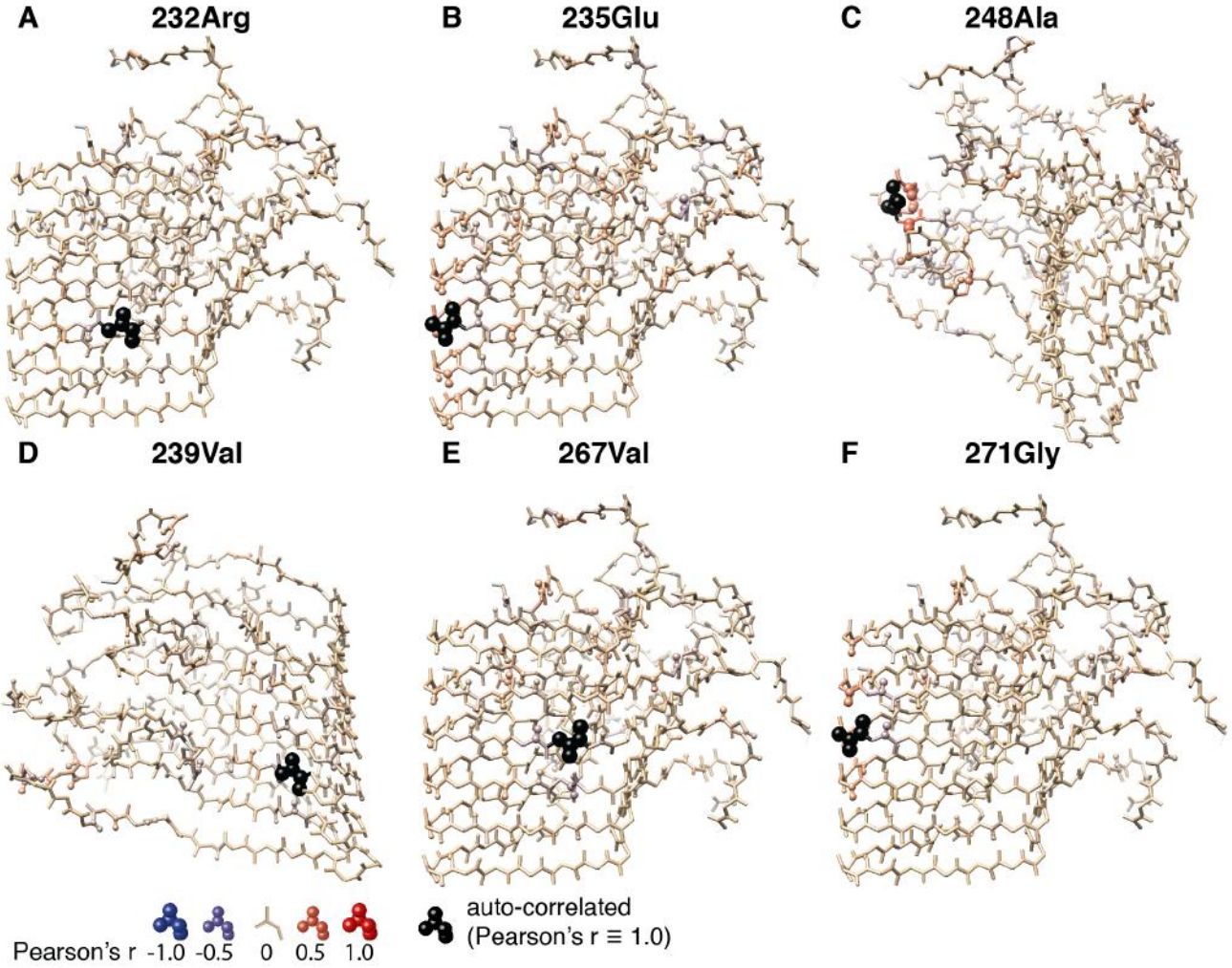

SI Fig. 21. Correlation coefficients calculated for the total motion (full range of correlation times) for selected residues (AMBER force field). Elements have been normalized by the square-root of the corresponding diagonal elements. Red and blue coloring indicates positive and negative correlation, respectively (max/min: +/-0.8). The residue to which each plot corresponds is shown as black (and has a normalized value of 1).

7.6. Cross-correlation for GROMOS trajectory

We also perform cross-correlation analysis for the GROMOS trajectory, to compare the degree of cross-correlation to the AMBER results. The overall results are shown in SI Fig. 22, with cross-correlation to several residues plotted onto the HET-s trimer in SI Fig. 23 and SI Fig. 24.

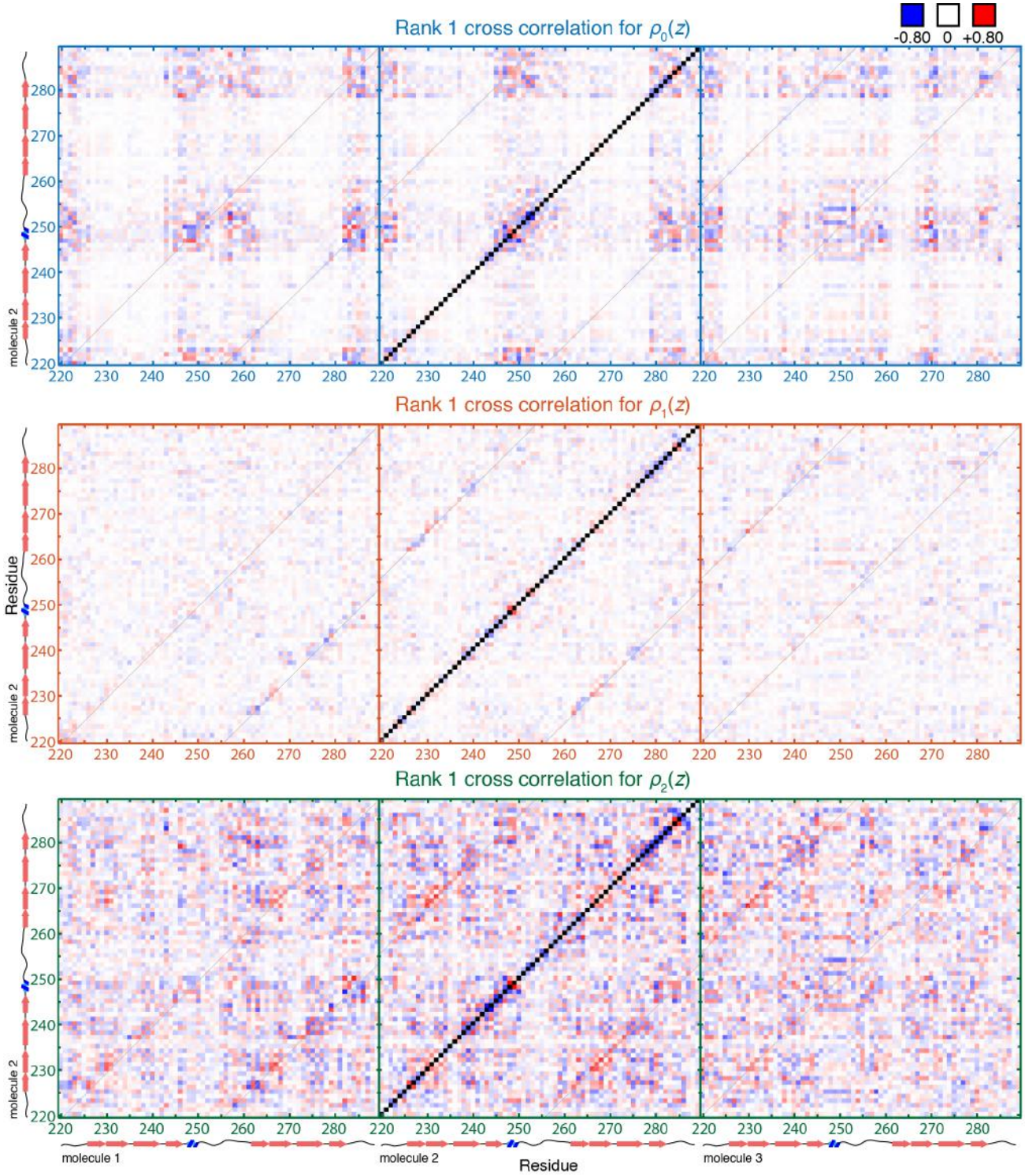

SI Fig. 22. Rank-1 correlated H–N bond motion between molecule 2 of the MD trajectory (y-axis) and all molecules (GROMOS force field). All elements are normalized by the square-root of the two corresponding diagonal elements (so the black, diagonal elements are all 1). All non-diagonal elements are coded with a blue-white-red color scale, corresponding to -0.80, 0, +0.80. Light grey lines through the plots indicate residues positioned exactly one layer above in the β-sheet (for example, residue 235 sits next to residue 271 of the same molecule, and 271 of the previous molecule. Two layers away corresponds to 235 from the two neighboring residues).

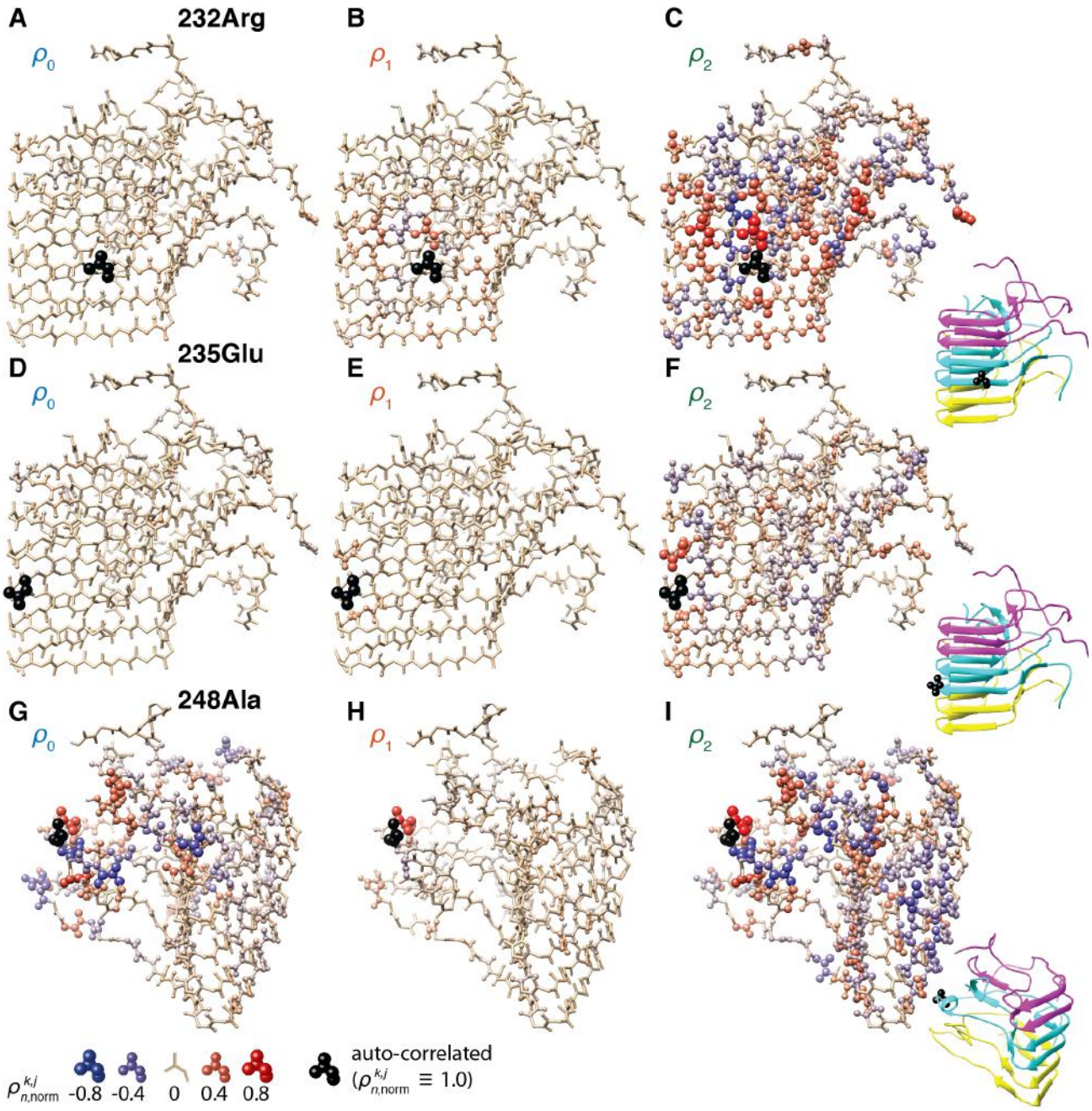

SI Fig. 23. Detector-specific correlation coefficients for several residues (rank-1), calculated from the GROMOS trajectory. Each subplot gives the correlation coefficients between an H–N bond of the middle HET-s(218-289) molecule (shown in black) to all other H–N bonds, for ρ_0, ρ_1, and ρ_2. The volume of each atom is proportional to $|\rho^{k,j}_{n,\mathrm{norm}}|$, whereas color coding also indicates the sign of $\rho^{k,j}_{n,\mathrm{norm}}$. All atoms in the same peptide plane as the H–N bond are sized and colored according to $\rho^{k,j}_{n,\mathrm{norm}}$ for better visibility. **A**-**C** are correlations to the H–N bond of residue 232Arg, **D**-**F** for residue 235Glu, and **G**-**I** for residue 248Ala. Yellow/cyan/magenta fibril plots (lower right) serve as a reference to see the overall fibril structure and orientation.

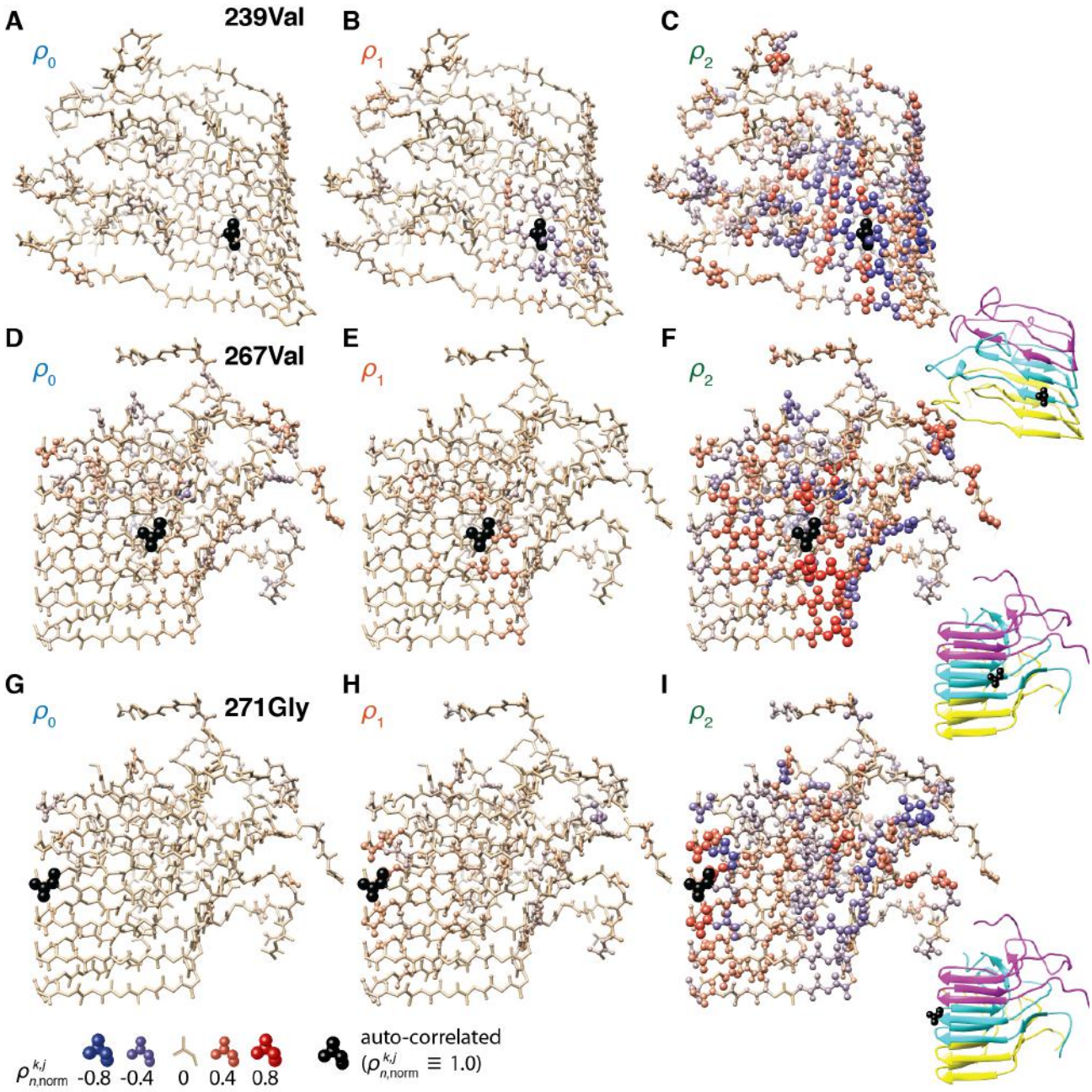

SI Fig. 24. Detector-specific correlation coefficients for several residues (rank-1), calculated from the GROMOS trajectory. Each subplot gives the correlation coefficients between an H–N bond of the middle HET-s(218-289) molecule (shown in black) to all other H–N bonds, for ρ_0, ρ_1, and ρ_2. The volume of each atom is proportional to $|\rho^{k,j}_{n,\mathrm{norm}}|$, whereas color coding also indicates the sign of $\rho^{k,j}_{n,\mathrm{norm}}$. All atoms in the same peptide plane as the H–N bond are sized and colored according to $\rho^{k,j}_{n,\mathrm{norm}}$ for better visibility. **A**-**C** are correlations to the H–N bond of residue 239Val, **D**-**F** for residue 267Val, and **G**-**I** for residue 271Gly. Yellow/cyan/magenta fibril plots (lower right) serve as a reference to see the overall fibril structure and orientation.

Note that the large degree of correlation in the sensitive range of ρ_0 for 248Ala (SI Fig. 23G) is actually due to correlation at long correlation times. We can see this by defining a new ρ_0 that is only sensitive to short correlation times. This new sensitivity is shown in SI Fig. 25A, where we see that the resulting cross-correlation is almost zero for nearly all residue pairs shown in SI Fig. 25B.

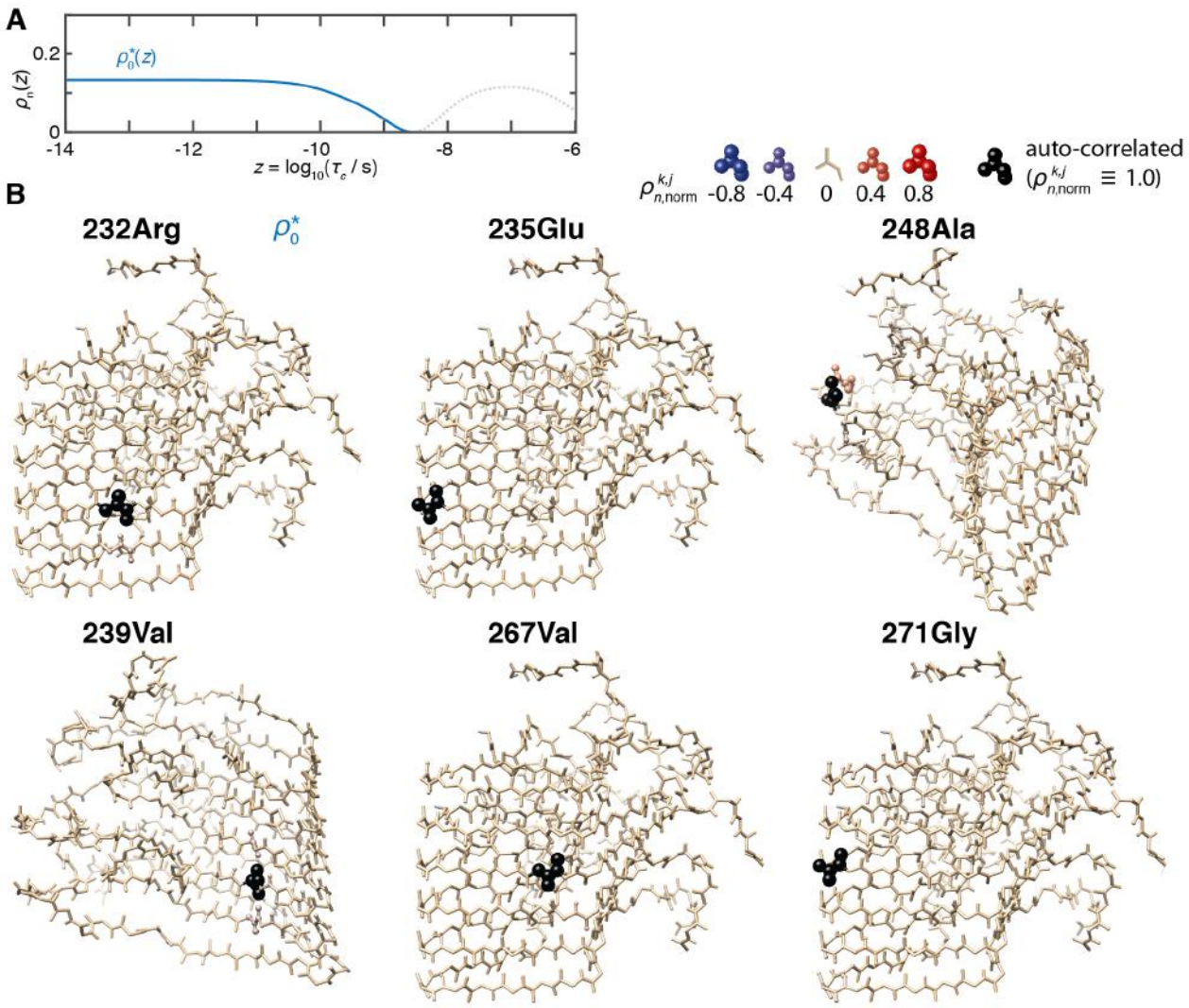

SI Fig. 25. Modified ρ_0 detector that is only sensitive to short correlation times. **A** shows the new detector sensitivity, where dotted line shows the region of the detector sensitivity that has been set to zero. **B** shows the cross-correlation for the same residues as shown in SI Fig. 23 and SI Fig. 24.

8. Analysis of microsecond motions

Data shown in main text Fig. 4 is re-plotted here, in order to show the amplitudes of the highest detector responses, which are cut off in the main text. These are also accompanied by high uncertainty, since the same peaks tend to have very broad linewidths and low amplitude in the experimental spectra.

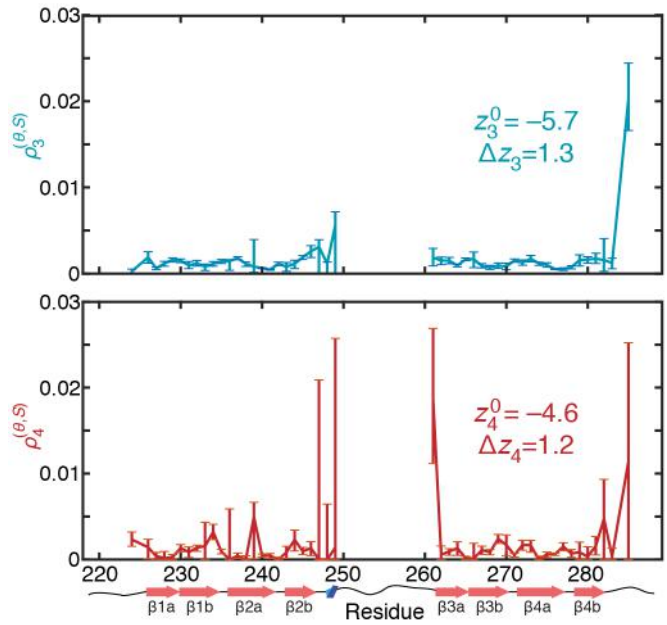

SI Fig. 26. Detector responses sensitive to µs motion ($\rho_3 : 10^{z^0} \sim 2\ \mu s$, $\rho_4 : 10^{z^0} \sim 25\ \mu s$). Detector responses $\rho_3^{(\theta,S)}$ and $\rho_4^{(\theta,S)}$ are shown, where the sensitivities of ρ_3 and ρ_4 are given in main text Fig. 4A. Note that this is the same plot as main text Fig. 4B, with an expanded *y*-axis to show the detectors with the highest responses.

9. References

[1] A. A. Smith, M. Ernst, B. H. Meier, *J. Chem. Phys.* **2018**, *148*, 045104.
[2] A. A. Smith, M. Ernst, B. H. Meier, difrate.sourceforge.net, **2018**.
[3] A. A. Smith, E. Testori, R. Cadalbert, B. H. Meier, M. Ernst, *J. Biomol. NMR* **2016**, *65*, 171-191.
[4] J. Dolenc, B. H. Meier, V. H. Rusu, W. F. van Gunsteren, *Phys. Chem. Chem. Phys.* **2016**.
[5] A. Lange, Z. Gattin, H. Van Melckebeke, C. Wasmer, A. Soragni, W. F. Gunsteren, B. H. Meier, *ChemBioChem* **2009**, *10*, 1657-1665.
[6] N. Schmid, A. P. Eichenberger, A. Choutko, S. Riniker, M. Winger, A. E. Mark, W. F. van Gunsteren, *Eur. Biophys. J.* **2011**, *40*, 843-856.
[7] a) K. Lindorff-Larsen, S. Piana, K. Palmo, P. Maragakis, J. L. Klepeis, R. O. Dror, D. E. Shaw, *Proteins* **2010**, *78*, 1950-1958; b) V. Hornak, R. Abel, A. Okur, B. Strockbine, A. Roitberg, C. Simmerling, *Proteins* **2006**, *65*, 712-725.
[8] H. Van Melckebeke, C. Wasmer, A. Lange, E. AB, A. Loquet, A. Böckmann, B. H. Meier, *J. Am. Chem. Soc.* **2010**, *132*, 13765-13775.
[9] W. F. van Gunsteren, H. J. C. Berendsen, *Angew. Chem. Int. Ed.* **1990**, *29*, 992-1023.
[10] R. W. Hockney, *Methods Comput. Phys.* **1970**, *9*, 136-210.
[11] H. J. C. Berendsen, J. P. M. Postma, W. F. van Gunsteren, J. Hermans, *Intermolecular Forces* **1981**, *14*, 331-342.
[12] H. J. C. Berendsen, J. P. M. Postma, W. F. van Gunsteren, A. DiNola, J. R. Haak, *J. Chem. Phys.* **1984**, *81*, 3684-3690.
[13] I. G. Tironi, R. Sperb, P. E. Smith, W. F. van Gunsteren, *J. Chem. Phys.* **1995**, *102*, 5451-5459.
[14] T. N. Heinz, W. F. van Gunsteren, P. H. Hünenberger, *J. Chem. Phys.* **2001**, *115*, 1125-1136.
[15] J.-P. Ryckaert, G. Ciccotti, H. J. C. Berendsen, *J. Comput. Phys.* **1977**, *23*, 327-341.
[16] a) M. J. Abraham, T. Murtola, R. Schulz, S. Páll, J. C. Smith, B. Hess, E. Lindahl, *SoftwareX* **2015**, *1-2*, 19-25; b) H. J. C. Berendsen, D. van der Spoel, R. van Drunen, *Comput. Phys. Commun.* **1995**, *91*, 43-56.
[17] W. L. Jorgensen, J. Chandrasekhar, J. D. Madura, R. W. Impey, M. L. Klein, *J. Chem. Phys.* **1983**, *79*, 926-935.
[18] T. Darden, D. York, L. Pedersen, *J. Chem. Phys.* **1993**, *98*, 10089-10092.
[19] B. Hess, H. Bekker, H. J. C. Berendsen, J. G. E. M. Fraaije, *J. Comput. Chem.* **1997**, *18*, 1463-1472.
[20] a) S. A. Showalter, R. Brüschweiler, *J. Chem. Theory Comput.* **2007**, *3*, 961-975; b) S. F. Lienin, T. Bremi, B. Brutscher, R. Brüschweiler, R. R. Ernst, *J. Am. Chem. Soc.* **1998**, *120*, 9870-9879.
[21] E. R. Henry, A. Szabo, *J. Chem. Phys.* **1985**, *82*, 4753.

[22] P. Bernado, M. Blackledge, *J. Am. Chem. Soc.* **2004**, *126*, 4907-4920.
[23] D. A. Case, *J. Biomol. NMR* **1999**, *15*, 95-102.
[24] M. Ottiger, A. Bax, *J. Am. Chem. Soc.* **1998**, *120*, 12334-12341.
[25] A. N. Tikhonov, V. I. A. Arsenin, *Solutions of Ill-Posed Problems*, Winston, Washington, DC, **1977**.
[26] W. H. Press, S. A. Teukolsky, W. T. Vetterling, B. P. Flannery, *Numerical Recipes*, 3rd ed., Cambridge University Press, New York, NY, USA, **1985**.
[27] a) L. Mollica, M. Baias, J. R. Lewandowski, B. J. Wylie, L. J. Sperling, C. M. Rienstra, L. Emsley, M. Blackledge, *J. Phys. Chem. Lett.* **2012**, *3*, 3657-3662; b) N. Salvi, A. Abyzov, M. Blackledge, *J. Phys. Chem. Lett.* **2016**, *7*, 2483-2489; c) T. Bremi, R. Brüschweiler, *J. Am. Chem. Soc.* **1997**, *119*, 6672-6673; d) Y. Xue, N. R. Skrynnikov, *J. Am. Chem. Soc.* **2011**, *133*, 14614-14628.
[28] G. Lipari, A. Szabo, *J. Am. Chem. Soc.* **1982**, *104*, 4546-4559.
[29] A. A. Smith, M. Ernst, B. H. Meier, F. Ferrage, *arXiv:1812.01890* **2018**.
[30] a) J. J. Prompers, R. Brüschweiler, *J. Am. Chem. Soc.* **2001**, *123*, 7305-7313; b) J. J. Prompers, R. Brüschweiler, *J. Am. Chem. Soc.* **2002**, *124*, 4522-4534.
[31] Y. Gu, D.-W. Li, R. Brûschweiler, *J. Chem. Theory Comput.* **2014**, *10*, 2599-2608.
[32] N. Salvi, A. Abyzov, M. Blackledge, *Angew. Chem. Int. Ed.* **2017**, *56*, 14020-14024.